THE THIOL-ENE ENCAPSULATION AND PHOTO-PHYSICAL CHARACTERIZATION OF COLLOIDAL SILICON NANOCRYSTALS SYNTHESIZED WITH Si_6H_{12} USING NON-THERMAL PLASMA REACTOR

A Dissertation
Submitted to the Graduate Faculty
of the
North Dakota State University
of Agriculture and Applied Science

By

Mahmud Ayad Sefannaser

In Partial Fulfillment of the Requirements
for the Degree of
DOCTOR OF PHILOSOPHY

Major Program:
Physics

July 2020

Fargo, North Dakota

North Dakota State University

Graduate School

Title

THE THIOL-ENE ENCAPSULATION AND PHOTO-PHYSICAL CHARACTERIZATION OF COLLOIDAL SILICON NANOCRYSTALS SYNTHESIZED WITH Si_6H_{12} USING NON-THERMAL PLASMA REACTOR

By

Mahmud Ayad Sefannaser

The Supervisory Committee certifies that this ***disquisition*** complies with North Dakota State University's regulations and meets the accepted standards for the degree of

DOCTOR OF PHILOSOPHY

SUPERVISORY COMMITTEE:

Erik Hobbie
Chair

Alan Denton

Yongki Choi

Danling Wang

Approved:

02/23/2021
Date

Sylvio May
Department Chair

ABSTRACT

Silicon nanocrystals (SiNCs) are nanometer-sized semiconducting materials. Their small size endows them with unique photophysical properties. Efficient photoluminescence (PL) from silicon nanocrystal (SiNC) composites has important implications for emerging solar-energy collection technologies, yet a detailed understanding of PL relaxation in non-colloidal SiNCs is still materializing. In this dissertation, we examine the photophysical properties of silicon nanocrystal/off-stoichiometry thiol-ene composites (SiNCs/OSTE hybrids).

The dissertation begins with an introduction to the photophysical properties of SiNCs, their photophysical properties, how SiNC/polymer composites are made, the various SiNC preparation techniques, and the most likely application areas for these nanocrystals. A description of experimental methods such as PL spectroscopy and transmission electron microscopy (TEM) follows, and SiNC/OSTE polymer preparation methods are then explained in detail.

In the first study, TEM and photophysical characterization were performed on selected polydisperse SiNCs samples. These samples were synthesized in a nonthermal plasma reactor, using Si_6H_{12} as precursor, and functionalized with R (where R is 1-dodecene). These SiNCs were dispersed in mesitylene:1-dodecene (5:1) as a colloid. Optical absorption, quantum efficiency, and PL lifetime of SiNCs were then investigated, as well as the relationship between quantum yield, lifetime, and PL peak.

In the second study, we selected samples for size separation via the density gradient ultracentrifugation method (DGU). We successfully applied this technique to separate silicon nanocrystals with sizes from 2 nm to 4 nm from the ensemble samples using an engineered

density medium layer stack, and photophysical characterization was performed on the DGU size–separated SiNCs.

Lastly, we explored details of PL relaxation in photo-polymerized off-stoichiometric polymer/nanocrystal hybrids. We found time- and air-stable emission from dilute composites with up to 70% QY, and we investigated PL relaxation in the parameter space of nanocrystal size and temperature. In light of previous work, our results reveal similarities between the impacts of crosslinking and cooling to cryogenic temperature, but of which are characterized by a relative reduction in the available of phonons.

ACKNOWLEDGMENTS

I would like to wholeheartedly express my gratitude to my advisor Dr. Erik Hobbie for his continued support of my research and for letting me explore new areas in experimental nanotechnology science. I am very appreciative that was always able to find time to discuss the research, provide feedback and guidance. His interest and support for me throughout this period always motivated me to stand up and go on. I would like to thank my committee members Dr. Alan Denton, Dr. Yongki Choi, and Dr. Danling Wang for taking their time to review and evaluate this work, despite how busy their schedules were.

I would like to appreciate Dr. Sylvio May and Dr. Alan Denton for their help and advice to support me during my Ph.D and after completing my Ph.D. study. I would like to give special thanks to Paul Omernik as well for being great guide for me during my role as GTA in the Department of Physics, NDSU. Dr. Sylvio May, as the chair of the department and Dr. Mila Kryjevskaia, remarkably helped me to enhance both my teaching skills and techniques since I started teaching my first course for college students. I am very grateful to them and the staff members, and my colleagues at the Department of Physics for supporting me throughout my academic study. I am especially thankful to NDSU for providing me graduate assistantships during my last semesters.

I would like to express my appreciation for Dr. Alan Denton, Dr. Erik Hobbie, and Dr. Andrei Kryjevski from NDSU, and Dr. Yen Lee Loh, and Dr. Willioam Schwalm from UND for teaching me graduate-level Physics courses. Dr. Loh's help and guidance continued even though I was transferred from UND to NDSU.

I would like to take this opportunity to express a special gratitude and appreciation to Dr. Samuel Brown, Dr. Todd Pringle, Kenneth Anderson, Salim Thomas, and Reed Petersen for their support and integrated work as a one group under the guidance of Dr. Hobbie.

I am thankful to friends of mine who always support me even though there are thousands of miles between us. Many thanks to my wife, Raja, for her patience and encouragement throughout my doctoral study.

DEDICATION

This work is dedicated to both my father and my mother who taught me how to love knowledge, may their souls rest in peace, to my wife Raja for her support, to my children, and to all of my brothers and sisters.

TABLE OF CONTENTS

LIST OF TABLES

LIST OF FIGURES

LIST OF ABBREVIATIONS

Si	Silicon
SiNCs	Silicon Nanocrystals
QDs	Quantum dots
HOMO	Highest Occupied Molecular Orbital
LUMO	Lowest Unoccupied Molecular Orbital
eV	Electron volt
LED	Light Emitting Diode
TNT	Trinitrotoluene
PETN	Pentaerythritol
RD	Royal Demolition Explosive
NREL	Renewable Energy Laboratory
RF	Radio Frequency
IR	Infrared
HSQ	Hydrogen Silsesquioxane
UV	Ultraviolet
VIS	Visible
NIR	Near-Infrared
PMT	Photomultiplier tube
HRTEM	High-Resolution Transmission Electron Microscopy
TEM	Transmission Electron Microscopy
PDI	Polydispersity index
PL	Photoluminescence
QY	Quantum Yield
PL-QY	Photoluminescence Quantum Yield

QYPL .....Quantum Yield of Photoluminescence

OSTE.....Off-stoichiometric thiol-ene

DGU .....Density Gradient Ultracentrifugation

LIST OF APPENDIX FIGURES

CHAPTER 1. INTRODUCTION AND BACKGROUND

1.1. The motive behind studying silicon nanocrystals

A silicon nanocrystal (SiNC) is made up of a few tens to a few thousands of silicon (Si) atoms and is typically 1-10 nm in size. My motivation for this subject stems from the desire to study the fundamental physics of something that is useful in technology, and to use the non-intuitive and unusual outcomes of quantum mechanics in order to construct systems that benefit from non-Newtonian effects. Silicon nanocrystals are a suitable candidate for such studies because they are interesting for applied physics. The SiNCs small sizes make them an appropriate system to build an optically active nanocomposite material and study the effects of quantum confinement, to investigate the homogenous broadening, and to exploit the photophysical characteristics to engineer SiNC/OSTE nanocomposites.

1.2. Photoluminescence of silicon nanocrystals

When Jöns Jakob Berzelius first isolated silicon (Si) in 1823, he helped usher in an entirely new field of semiconductor technology.[1] Historically, Si was predicted by Antoine Lavoisier in 1787 and named by Thomas Thomson in 1817.[1,2] Lavoisier and Thomson believed that silicon was a nonmetal element similar to carbon. Then, in 1906 Si was considered to be a semiconducting material and was used to make first silicon semiconductor device (silicon radio detector).[3,4]

The most essential features of Si are that it accounts for 28% of the earth's crust, which makes it the second-most abundant element; it is considered a nontoxic component; and it is regarded as a low-cost material. All of these features make Si the material most used to produce electronic devices and circuits. The difficulty regarding Si is that in bulk form Si performs poorly as a light emitter because of its indirect bandgap. Recently, researchers have managed to improve

the photophysical properties of Si by reducing its size from bulk Si to silicon nanocrystals (SiNCs), bringing about interesting new properties and functionalities.[5,6]

The first examples of nanocrystals were discovered in a glass matrix by Alexey Ekimov in 1981.[5] Then in 1990 SiNCs emerged as an important form of silicon (Si). Since then, the size of SiNCs has become an important factor for controlling their photophysical properties. SiNCs are tiny pieces of crystalline Si that consist of a few tens to a few thousands of Si atoms with typical dimensions of 1-10 nm, as shown in **Figure 1.1a**.[7] SiNCs are also called silicon quantum dots, where the term quantum dot was first coined by Mark Reed.[6] These quantum dots are not completely homogeneous from the core to the surface. Rather, they are made up of three layers: surface, subsurface, and core silicon regimes, as sown in **Figure 1.1b**.[8] This structure led SiNCs to attract considerable interest with respect to their new photophysical properties as next-generation quantum dots.

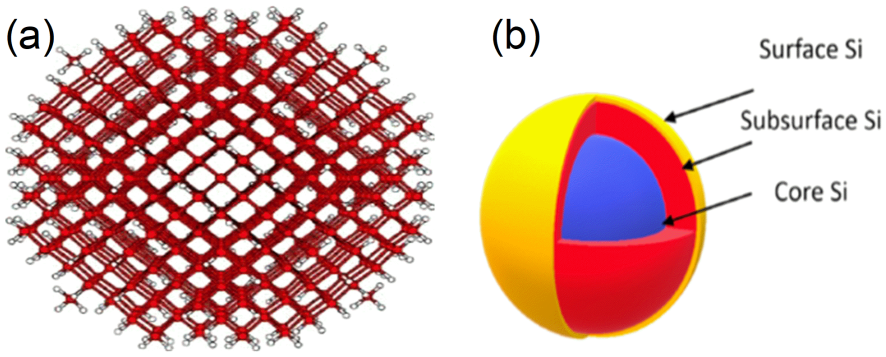

Figure 1.1: (a) Silicon nanocrystal. The interior of the nanocrystal has the structure of crystalline silicon. Taken from Ref. [7]. (b) Silicon nanoparticle (quantum dot). Taken from Ref. [8]

The unique photophysical properties of zero-dimensional SiNCs have attracted broad interest since 1990 when Canham discovered that porous silicon can exhibit efficient room-temperature photoluminescence (PL) at visible energies above the bulk silicon bandgap.[9] The PL properties of SiNCs are attributed to quantum confinement.[10]

Quantum confinement is explained using the term bandgap, which is used to characterize the properties of semiconductors. The bandgap is the difference in energy between the valence band and the conduction band of a semiconducting material, and includes energy levels as shown in **Figure 1.2**. For semiconductors, the bandgap is in the range from 1 to 3 eV.[11] With bulk silicon, for example, the bandgap is 1.12 eV at room temperature. However, SiNCs are unique because their bandgap is entirely different, as shown in **Figure 1.2**. When a semiconductor material reaches the nanoscale level to form nanocrystals, its dimensions decrease to the order of the Bohr exciton radius. Consequently, the bandgap begins to evolve: the indirect minima at the X point of the Brillion zone starts to increase in energy while the direct transition at the Γ point of the Brillion zone begins to decrease, as indicated in **Figure 1.3**.[12] As a result, silicon's indirect bandgap is driven to the visible range because of quantum confinement.

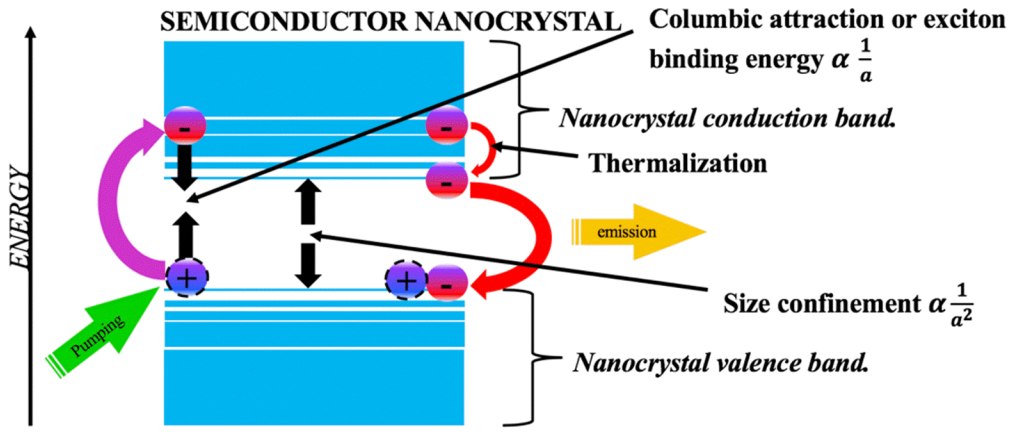

Figure 1.2: Energy bandgap of a semiconductor nanocrystal.

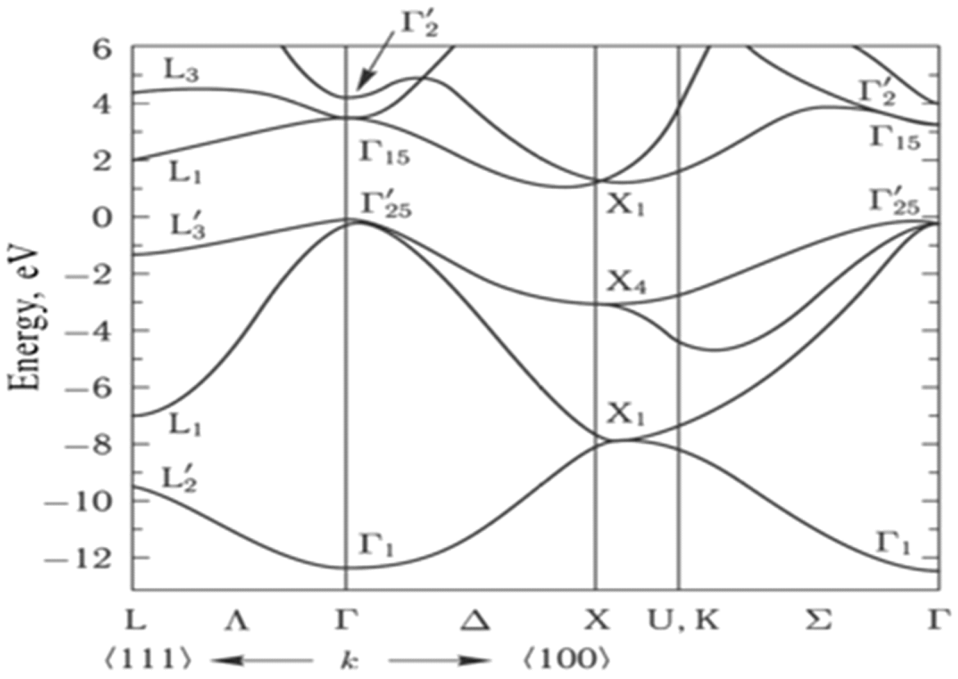

Figure 1.3: The bandgap structure of silicon. Taken from Ref. [12]

Furthermore, quantum confinement is related to squeezing the wavefunctions of the electron-hole pairs within the nanocrystal in real space, resulting in a broadening of the wavefunction in momentum space according to the Heisenberg uncertainty principle. The overlap between the electron and hole wavefunction is increased, as shown in **Figure 1.4a**. Therefore, the probability of direct radiative recombination between an electron and a hole improves. In the case of the larger nanocrystals, as in **Figure 1.4b**, the help of a phonon is needed to conserve momentum. When the nanocrystals are smaller than the Bohr exciton radius of silicon (around 5 nm), they can be thought of as molecules, where the valence band and conduction band evolve into the highest occupied molecular orbital (HOMO) and the lowest unoccupied molecular orbital (LUMO).[11]

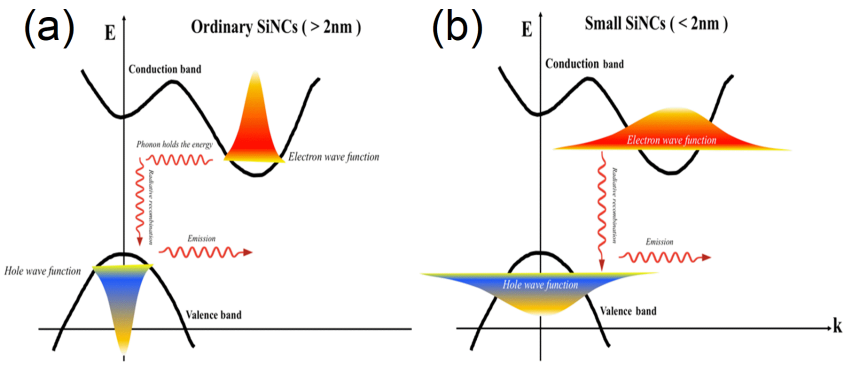

Figure 1.4: Radiative recombination in large (a) and small (b) indirect bandgap semiconductor crystals and the change in the electron and hole wavefunctions due to quantum confinement. Modified from Ref. [12]

1.3. The physics behind quantum confinement

The previous section mentions quantum confinement and how to use it to explain the PL properties of SiNCs. This section goes deeper into the underlying physics to understand the fundamental principles behind quantum confinement. The meaning of quantum confinement can be illustrated by the effective mass approximation of electrons and holes in a semiconductor and by examining the particle in a box problem, i.e., the effective mass of an electron and the effective mass of a hole in a one-dimensional infinite-potential well. Solutions to the time-independent Schrodinger equation provide discrete levels of energy with energies inversely proportional to the well width squared. In other words, the lower the well's width (i.e., the smaller the nanoparticle's size), the greater the ground state energy. Because the effective mass of the hole is negative in this approximation, this effect results in an increase in bandgap. In this section, I explain how quantum confinement is strongly related to an essential problem in quantum mechanics, which is a particle in an infinite spherical well. In this particular problem, the potential depends only on the distance between the particle and a defined center point and is zero inside the sphere and infinity outside the sphere.

The Schrödinger equation for an infinite spherical well has been studied in great detail. Because the potential energy inside the well is zero, the radial solutions are required to satisfy a boundary condition. The radial equation reduces to the spherical Bessel equation, which has irregular and regular solutions at the origin; the spherical Neumann functions $[\eta_l(\rho)]$ and the spherical Bessel functions $[j_l(\rho)]$ as shown in **Figures 1.5a and 1.5b,** respectively. Subjecting these terms to the usual boundary condition for the infinite square well, and including the electron-hole interaction, gives the energy eigenvalues and the corresponding bandgap:

$$E_g = E_0 + \frac{\hbar^2}{2\mu}\left(\frac{n_r\pi}{a}\right)^2 - \frac{1.8\,e^2}{4\,\pi\varepsilon\varepsilon_0 a}. \tag{1.1}$$

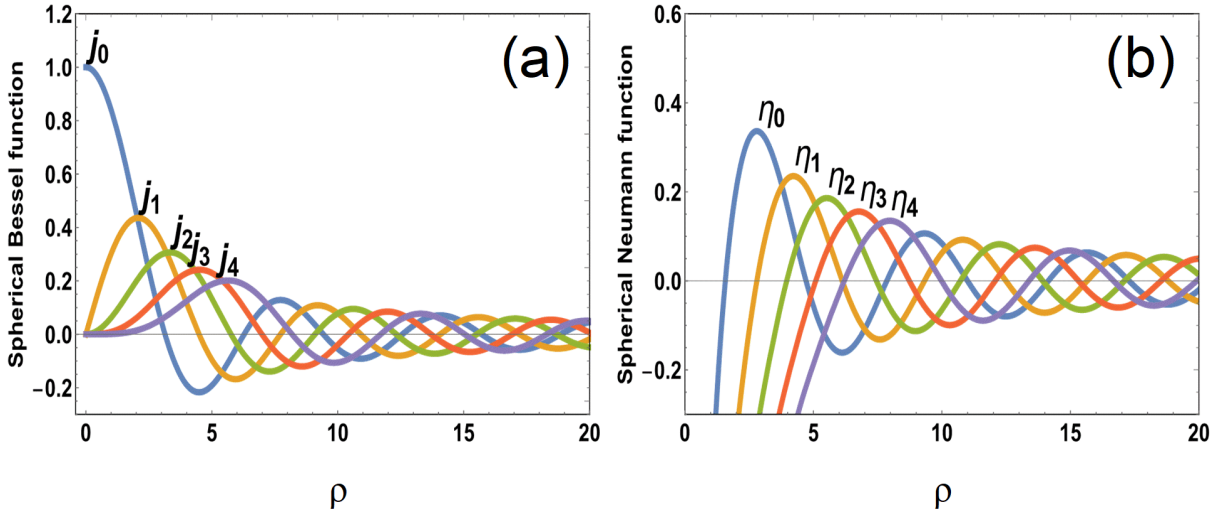

Figure 1.5: Spherical Neumann function (a) and Spherical Bessel function (b) plotted for four roots.

The first term in this expression is the silicon bandgap energy, which is 1.12 eV. The second term is from size confinement in a spherical box (quantum-confinement) and the third term is the Coulomb interaction energy between electron and hole. When plotted versus the diameter of the nanocrystal, the result is **Figure 1.6**, which tells us that by increasing the size of the nanocrystal, the optical bandgap energy decreases.

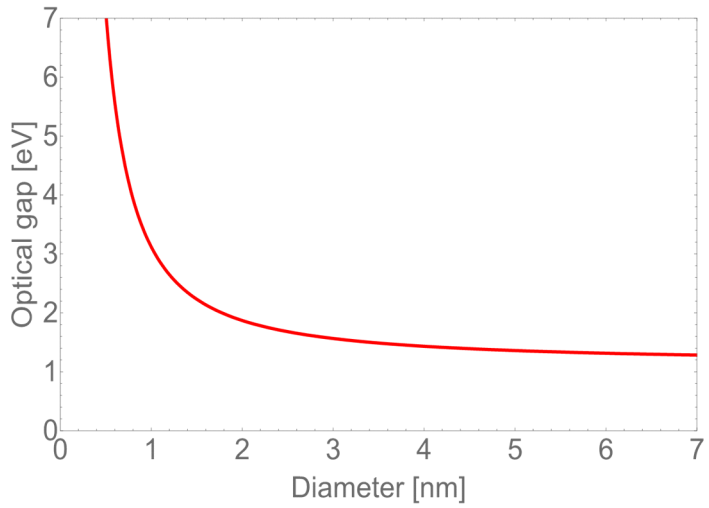

Figure 1.6: The graph represents Optical gap as a function of the nanocrystal size from Eq. (1.1).

1.4. Effect of size distribution on photoluminescence

As the number of potential applications increases, it becomes increasingly important to have a deep understanding of the size dependent optoelectronic, chemical, and biological properties of SiNCs. The goal is to generate high quality, colloidally stable, extremely monodisperse SiNCs in order to correctly characterize these properties. The measured PL spectra have intrinsically broad linewidth for SiNCs. Some of this breadth is due to size polydispersity, but mostly it derives from electron-phonon coupling in an indirect bandgap material.

1.5. Size-selective separation techniques

A somewhat narrower PL linewidth can be achieved by extracting monodisperse SiNCs from polydisperse SiNCs.[13] To do so, there are several available techniques that can be used to obtain monodisperse SiNCs. The following methods represent size-separation techniques that are available to purify nanoparticles.[14]

a. Size-selective precipitation.

b. Size separation using ultracentrifugation.

c. Size separation using electrophoresis.

d. Membrane filtration.

e. Size separation using a magnetic field.

The first and second techniques are the most effective methods for separating SiNCs by diameter. In this research, the method was limited to the ultracentrifugation technique (Appendix A). In particular, the density gradient ultracentrifugation (DGU) was used.

1.6. Surface defects and photoluminescence

Oxidation, which is one of the most problematic surface defects, can limit both the photophysical and structural properties of SiNCs. In particular, it can impact PL by lowering the quantum yield. This phenomenon can occur when SiNCs are exposed to the ambient environment. Even when the SiNC sample is stored in an O_2-free atmosphere, the oxidation process could happen due to exposure to ambient conditions when sealing the sample vial.[15] Having silicon-oxygen bonds on the surface can prevent SiNCs from achieving high quantum yield (QY) values because these bonds affect the bandgap.[16]

The bandgap can be changed because of the more massive distortion of surface bonds leading to surface states. The density of states is localized around the defect (e.g., doubly bonded oxygen) in the case of nanocrystals that are smaller than 3 nm.[17] It has been suggested that the doubly-bonded oxygen is the main factor responsible for decreasing the bandgap of small nanocrystals with sizes from 1 to 3.5 nm.[17,18] Other possible defects are hydroxyl groups and back-bonded oxygen (Si-OH and Si-O-Si, respectively). A theoretical study indicated that the spectra of SiNCs with either Si-OH or Si-O-Si are quite similar to the case of defect-free SiNCs.[19] However, the doubly-bonded defect has two peaks on the surface of the SiNC in a model with a 2-nm nanocrystal size. **Figure 1.7** shows how oxidation affects the bandgap and how surface states appear in the double bonded oxygen model.

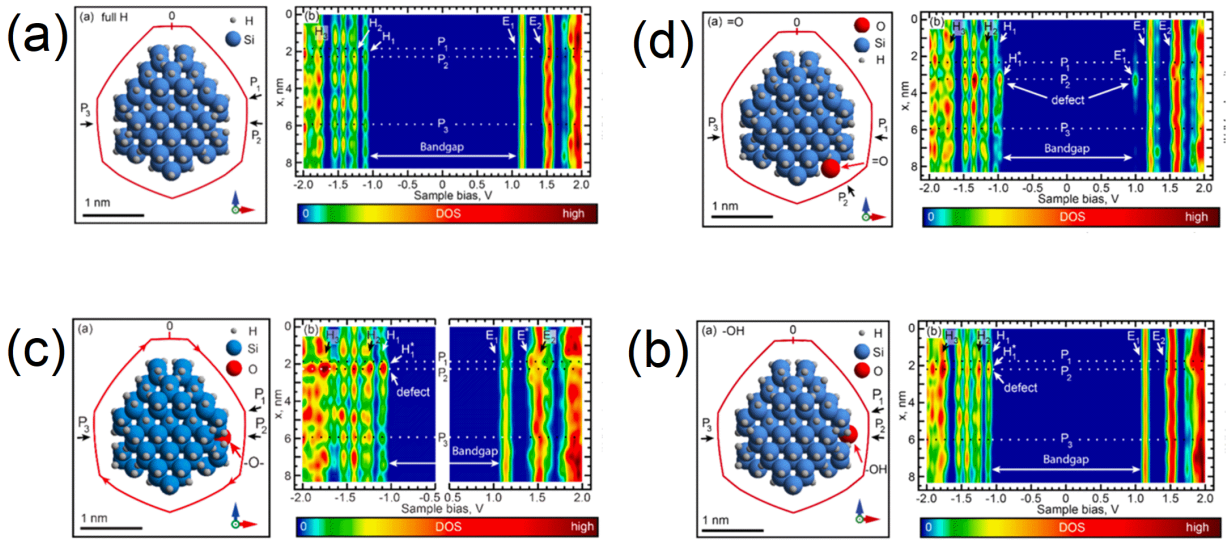

Figure 1.7: Theoretical density of states for a near-spherical model of a SiNC with (a) no defects, (b) Si=O, (c) Si-O-Si, and (d) Si-OH. Taken from Ref. [19]

To avoid defects in synthesized SiNCs, modifying both the surface and chemical composition is essential. For example, fully hydrogen-passivated SiNCs do not introduce surface states to the bandgap even in small nanocrystals. However, dangling bonds will continue to be a stumbling block because dangling bounds are also considered defects.[17-19] Therefore, the surface of SiNCs has been studied to enhance their resistance against oxidation and to improve their PL properties.[20] Alkene-passivated SiNCs are less prone to oxidation than entirely hydrogen-passivated SiNCs, which improves their photophysical properties.[19] However, alkene-passivated SiNCs are not a strong wall to stop the oxidation process because oxidation could occur slowly in an exposed sample.[20] This requires a new passivation technique to limit oxidation and possibly improve the photophysical properties.

1.7. SiNC/Polymer nanocomposite and photoluminescence

Making SiNC/Polymer hybrid materials is a promising way to shield SiNCs from exposure to ambient O_2 and water and thereby maintain stable photophysical properties and in particular impart photoluminescent stability. As SiNC size has a primary role in controlling the

luminescent properties, encapsulating SiNCs in a polymer matrix can help shield them from the environment. Even though polymers and SiNCs have individual properties that can be tuned independently, these components together can make attractive nanocomposites.[21-23] These nanocomposites bring new features based on the properties of the components, as well as the interactions between the SiNCs and polymers. Several methods have been established to make a hybrid material from quantum dots and polymers.[24-31]

Developing methods to produce SiNC/polymer nanocomposites with improved photoluminescence stability is important for many applications. Liu et al. used a physical blending of components approach to synthesize a nanocomposite from nanocrystals and poly-3-hexylthiophene (NC/P3HT) for use in photovoltaic devices.[24] Although this method has shown some promising advantages, it is ultimately hindered by the formation of nanocrystals clusters. This leads to the formation of a heterogeneous nanocomposites, while the nanocrystals are well shielded. Mitra et al. improved the homogeneity using the atmospheric micro-plasma approach.[25] This method helped coat SiNCs completely and improved homogeneity of the nanocomposite as well as the photoluminescence stability. Hessel et al. synthesized a nanocomposite material made of alkyl terminated SiNCs and poly(maleic anhy-dride) (amphiphilic polymer).[26] This hybrid material had photoluminescent stability under large pH ranges that makes it a promising choice for biological applications. Another method for synthesizing a SiNC/polymer hybrid is called reversible addition-fragmentation chain transfer (RAFT) polymerization.[27] The RAFT method applies polymerization with styrene, methyl methacrylate, hexyl acrylate, 4-vinylbenzyl chloride, and N-isopropylamide on the SiNC surface to achieve luminescence from the hybrid. This nanocomposite material showed a narrow size distribution and higher photoluminescence stability in potassium hydroxide compared with alkyl functionalized SiNCs. A

SiNC/polystyrene nanocomposite was reported to make a hybrid that is photoluminescent, homogeneous, and chemically stable.[28] A thermal reaction was used to induce the auto-initiated polymerization of styrene to form this nanocomposite. When the styrene radicals remove hydrogen from the SiNC surface, polystyrene-functionalized SiNCs are produced. The SiNC/polystyrene nanocomposite is stable under increasing temperatures up to 250 °C.[29] The refractive index of SiNC/polystyrene increases with increasing SiNC concentration.[30] A SiNC/polysiloxane nanocomposite was reported, and it had interesting features such as luminescence, extendibility, and transparency.[31] The siloxane linkages were used to assist a silicone elastomer to directly attach to the surface of SiNCs. SiNC/polysiloxane nanocomposites showed stable photoluminescence under solvent polarity and mechanical stress.

To conclude, unshielded SiNCs have a limited resistance to atmospheric oxidation, which weakens their photophysical properties. Therefore, effective methods must be considered to prevent oxidation. The most important proposal is the encapsulation of SiNCs in a polymer material, which in turn leads to the isolation of the SiNCs from ambient conditions and protection of the surface.

1.8. Synthesis of silicon nanocrystals

In general, there are two main methods to produce SiNCs. These methods can be divided into non-plasma techniques and plasma techniques.[20] These methods can be used to make SiNCs with different characteristics. For example, average particle size, the degree of crystallinity, and impurity content are some of the characteristics that SiNCs can have when the above-mentioned methods are used.

1.8.1. Synthesis of silicon nanocrystals using non-plasma techniques

The classification of synthesis methods for SiNCs covers many different approaches. In this dissertation, three methods are reviewed.[12]

(a) Ion implantation: Ion implantation is one of the most popular techniques to synthesize silicon nanocrystals. As shown in **Figure 1.8**, the instrument is quite complicated, yet basic physics rules are implemented to operate it. The silicon ions are accelerated toward a mass separation spectrometer, which removes the undesired species. Then, the silicon ions access the target chamber, which consists of specific conditions of temperature, high vacuum, and target position. Then, the implantation of silicon ions at very controlled depths in an SiO_2 matrix (target) begins, as in **Figure 1.8 a & b**. This step would be performed by controlling both the density and the energy of the ion beam. Finally, silicon nanocrystals are produced at various depths with a size around 2 nm.[12,20]

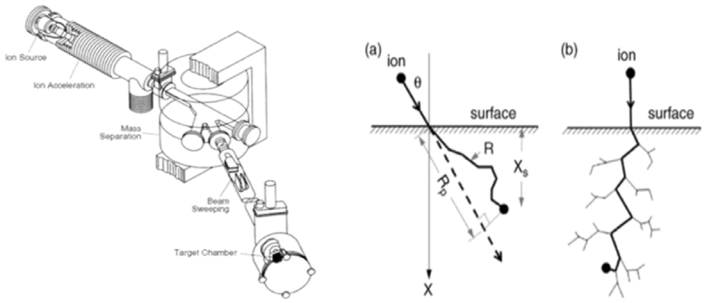

Figure 1.8: Schematic diagram of an ion- implantation instrument, left. (a) and (b) Schematic of possible implanted ion trajectory, right. Taken from Ref. [20]

(b) Laser ablation: This method is used extensively for the preparation of SiNCs. With this technique, a laser beam is utilized as the primary excitation source to vaporize the material from the surface of a single-crystal silicon wafer and generate clusters. The scattered SiNCs are deposited on a quartz substrate, as in **Figure 1.9**. The SiNCs that are produced using this technique have an average diameter of 4 to 5 nm.[12]

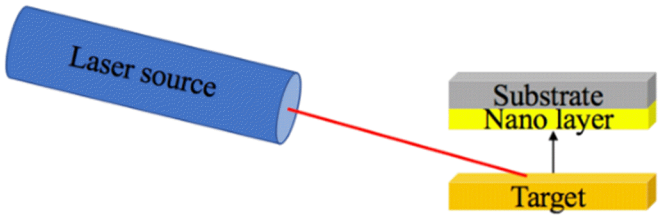

Figure 1.9: Schematic diagram of the laser- ablation setup.

(c) Using a beam of electrons to evaporate crystalline silicon: The first example of evaporating crystalline silicon with an electron beam was conducted by Lukashove and Bardakhonove in 1997.[12] The process is described as follows:

a. Evaporate a solid material in an electron beam.
b. Cool and coagulate the vapor-air mixture, with the condensation of material in the form of nanoparticles.
c. Capture and collect the resulting nanomaterial as a powder.

1.8.2. Synthesis of silicon nanocrystal using the plasma technique

In general, from the molecular interrelations point of view, matter can exist in four states: solid, liquid, gas, and plasma. Furthermore, the plasma can be divided into low-temperature plasma and high-temperature plasma. The low-temperature plasma technique can be used to synthesize SiNCs. As can be seen in **Figure 1.10a**, the low-temperature plasma is further classified into thermal plasma and cold plasma. Finally, the cold plasma is divided into plasma deposition and plasma treatment.[32] Cold plasma is generated in laboratories by using chambers under low pressure with an electric glow discharge. In addition, the radio frequency (RF) is critical to the formation of the cold plasma. **Figure 1.10b** shows a diagram of a typical parallel-plate plasma reactor.

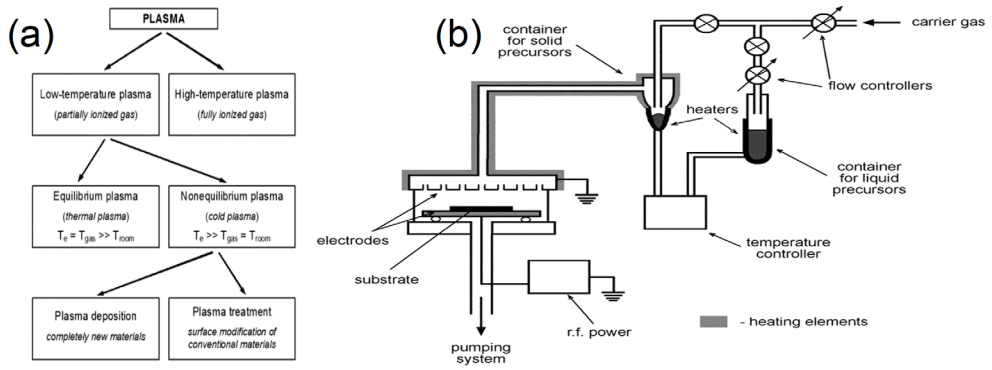

Figure 1.10: (a) Classification of the plasma types. Taken from Ref. [32] (b) A cartoon of parallel- plate cold plasma reactor. Taken from Ref. [32]

1.9. Applications

SiNCs are made of group IV Si atoms. SiNCs have unique physical and optical properties that can be altered by modifying their size or surface structure, doping them with impurity atoms, and embedding them in solid matrices. The semiconducting and non-toxicity features of Si make SiNCs a material compatible with the current needs of select application platforms.[33] Because SiNCs are materials that absorb and emit light based on their size, they are a suitable for many applications.[34-37] When SiNCs are pristine, monodisperse, and embedded in different polymers, they can provide nanocomposites with distinctive properties that can open up new applications. Controlling passivation can improve the optical properties of SiNCs.[37,38] Because SiNCs have unique photophysical properties, they have been investigated for applications such as light emitting diodes (LEDs), sensors, solar panels, sensitizers, and photonic circuits.[39-43]

Nanocrystal light-emitting diode systems (LEDs) are advancing rapidly, and it is now apparent that they can provide adequate brightness and color purity for screens and a variety of applications. As an example, plasma displays waste an extraordinary amount of energy relative to the required power to operate them. Hence, LEDs, which consume much less power, are an excellent choice to fabricate displays with higher efficiency. While these nanocrystal systems

have brilliant optical and electrical characteristics, the toxicity of materials such as CdSe remains a significant problem, especially when considering industrial scale-up.[44-47] Hence, non-toxic SiNCs with properties such as bright luminescence have become attractive emission materials for LEDs.[39-43] To achieve this goal, research efforts are still ongoing to realize LEDs made with SiNCs that are distinguished by both high performance and long life.

Another application for SiNCs is making PL-based sensors. Because SiNC-based sensors have high sensitivity, portability, rapid response, and low cost, they can provide highly effective performance.[48] SiNCs have the ability to exhibit rapid fluorescence quenching, which helps to detect some chemicals in the form of either solutions or vapors.[42] The SiNC paper-based sensor is applicable for detecting explosive solutions such as trinitrotoluene (TNT), pentaerythritol tetranitrate (PETN), and royal demolition explosive (RDX); these sensors are made by dip-coating filter paper in a concentrated toluene solution of SiNCs. The mechanism of detecting the mentioned chemicals depends on rapid fluorescence quenching, which arises from electron transfer from the SiNC to the chemical molecule. These sensors can also be used in biomedical applications, for example. This type of sensor does not interfere with molecules in living systems while showing selective dopamine detection at deficient dopamine concentration.[49] This makes SiNC paper-based sensors quite effective for detecting any particular molecule in both non-living and living systems.

Currently, the world needs a renewable energy source that does not adversely affect the environment. Solar energy has broad interest and appeal because it can be converted into one of the most useful forms of energy (electricity) by photovoltaic devices. Typical solar cells generate up to one electron per incoming photon, but SiNCs have been reported to exhibit multiple exciton generation.[41] This created a turning point for interest in SiNCs, as it may lead to

improved solar cell efficiency.[41] Blue and ultraviolet light have more energy compared to the rest of the solar spectrum, and these are the wavelengths where multiple exciton generation has been observed. According to National Renewable Energy Laboratory (NREL), solar cells made of SiNCs could theoretically convert more than 40 % of the energy of incident sunlight.[50] However, today's flat rooftop solar panels typically achieve 20% to 30% efficiency. Encapsulating SiNCs in off-stoichiometric thiol-ene polymer composites has been proposed as a way to improve PL QY,[51] and SiNC/OSTE hybrid materials are an excellent candidate for fabricating luminescent solar concentrators (LSCs). A LSC is a device that is used to concentrate sunlight to enhance the efficiency of solar cells. However, SiNCs must have high QY to be useful for making LSCs. All of these mentioned reasons make SiNCs a potential candidate for use in the solar energy industry.

SiNCs can also potentially be used to treat cancer by making sensitizers based on radio frequency (RF). The application of RF can induce hyperthermia, which increases the temperature of SiNCs[49]. If the SiNCs are distributed around cancer cells, increasing the temperature can kill these cells. The only problem here is that the SiNC surface is very sensitive to aqueous environments, which can lower the QY. This in turn emphasizes the importance of encapsulating SiNCs in a non-toxic substance, which preserves the SiNCs' optical properties. There were many attempts to make SiNC/polymer nanocomposites that can be used in biology, especially in magnetic resonance imaging.[34,35,36] If a polymer has been discovered that can encapsulate SiNCs and preserve photophysical properties, as well as being non-toxic, SiNCs have the potential to be used in cancer treatment and bioimaging.

Recently, Si has become an attractive material for monolithic integrated photonic circuits with a wide range of applications.[34] In 2000, the first work on the optical gain of SiNCs was

published.[52] An alternative approach was used to improve the optical gain of SiNCs.[52-54] This method can either reduce non-radiative centers or enhance the population inversion. Wang et al. reported that SiNCs can be used as an active medium at visible wavelengths to efficiently sensitize erbium ions for light amplification in the infrared (IR) region.[40] Optically pumped all-SiNC laser devices have been recently reported with encouraging results for the development of SiNC-based lasers.[40] The active SiNC layer was made with hydrogen silsesquioxane (HSQ) and then hydrogen passivated using high-pressure. The SiNC-based laser, which was optically pumped with femtosecond pulses, may open routes to reducing the lost heat energy due to the usual rise in temperature of lasers made of SiNCs.

In conclusion, SiNCs have demonstrated their potential importance for a broad scope of applications and there is still plenty of room to obtain precisely controlled SiNC characteristics, discover new phenomena, and make critical contributions.

1.10. Bibliography

1. Lavoisier, Traité Élémentaire de Chimie, (Paris, France: Cuchet), vol. 1, page 17, **1789**
2. Thomson, T. A System of Chemistry in Four Volumes, 5th ed., vol. 1, **1817**
3. Canham, L. T, Silicon Quantum Wire Array Fabrication by Electrochemical and Chemical Dissolution of Wafers. *Applied Physics Letters.* **1990**, 57 (10), 1046-1048.
4. Cullis, A. G.; Canham, L. T, "Visible-Light Emission Due to Quantum Size Effects in Highly Porous Crystalline Silicon. *Nature*. **1991**, 353 (6342), 335-338.
5. Ekimov, AI; Onushchenko, AA. Quantum size effects in the optical spectra of semiconductor microcrystals. *Soviet Physics Semiconductors-USSR.* **1981**, 16, (7), 775–778.
6. Reed, M.; Randall, J.; Aggarwal, R.; Matyi, R.; Moore, T.; Wetsel, A. Observation of Discrete Electronic States in a Zero-Dimensional Semiconductor Nanostructure. *Phys. Rev. Lett.* **1988**, *60* (6), 535–537.
7. Chelikowsky, J. R.; Zayak, A. T.; Chan, T.-L.; Tiago, M. L.; Zhou, Y.; Saad, Y. Algorithms for the Electronic and Vibrational Properties of Nanocrystals. *J. Phys.: Condens. Matter* **2009**, *21* (6), 064207.

8. Thiessen, A. N.; Ha, M.; Hooper, R. W.; Yu, H.; Oliynyk, A. O.; Veinot, J. G. C.; Michaelis, V. K. Silicon Nanoparticles: Are They Crystalline from the Core to the Surface? *Chem. Mater.* **2019**, *31* (3), 678–688.

9. A. G, Cullis; and L.T. Canham. Visible Light Emission Due to Quantum Size Effects in Highly Porous Crystalline Silicon, *Letters to Nature*. **1991**, 353, 335-338.

10. Rao, C. N. R.; Kulkarni, G. U.; Thomas, P. J.; Edwards, P. P. Size-Dependent Chemistry: Properties of Nanocrystals. *Chem. Eur. J.* **2002**, 8 (1), 28-35

11. Smith, A. M.; Nie, S. Semiconductor Nanocrystals: Structure, Properties, and Band Gap Engineering. *Acc. Chem. Res.* **2010**, *43* (2), 190–200.

12. Ischenko, A. A.; Fetisov, G. V.; Aslalnov, L. A. *Nanosilicon: Properties, Synthesis, Applications, Methods of Analysis and Control*, 0 ed.; CRC Press, **2014**.

13. Sychugov, I.; Fucikova, A.; Pevere, F.; Yang, Z.; Veinot, J. G. C.; Linnros, J. Ultranarrow Luminescence Linewidth of Silicon Nanocrystals and Influence of Matrix. *ACS Photonics,* **2014**, *1* (10), 998–1005.

14. Yasushige Mori, "Size-Selective Separation Techniques for Nanoparticles in Liquid," *KONA Powder and Particle Journal*, **2015**, 32, 102-114.

15. Elbaradei, A.; Brown, S. L.; Miller, J. B.; May, S.; Hobbie, E. K. Interaction of Polymer-Coated Silicon Nanocrystals with Lipid Bilayers and Surfactant Interfaces. *Phys. Rev. E* **2016**, *94* (4), 042804.

16. Zhou, Z.; Brus, L.; Friesner, R. Electronic Structure and Luminescence of 1.1- and 1.4-Nm Silicon Nanocrystals: Oxide Shell versus Hydrogen Passivation. *Nano Lett.* **2003**, *3* (2), 163–167.

17. Kocevski, V.; Eriksson, O.; Rusz, J. Size Dependence of the Stability, Electronic Structure, and Optical Properties of Silicon Nanocrystals with Various Surface Impurities. *Phys. Rev. B* **2015**, *91* (12), 125402.

18. Pi, X.; Wang, R.; Yang, D. Density Functional Theory Study on the Oxidation of Hydrosilylated Silicon Nanocrystals. *Journal of Materials Science & Technology* **2014**, *30* (7), 639–643.

19. Kislitsyn, D. A.; Kocevski, V.; Mills, J. M.; Chiu, S.-K.; Gervasi, C. F.; Taber, B. N.; Rosenfield, A. E.; Eriksson, O.; Rusz, J.; Goforth, A. M.; et al. Mapping of Defects in Individual Silicon Nanocrystals Using Real-Space Spectroscopy. *J. Phys. Chem. Lett.* **2016**, *7* (6), 1047–1054.

20. Lorenzo, P. and Rasit, T. Silicon Nanocrystals; Mörlenbach: Wiley-VCH Verlag, **2010**.

21. Shi, W.; Zeng, H.; Sahoo, Y.; Ohulchanskyy, T. Y.; Ding, Y.; Wang, Z. L.; Swihart, M.; Prasad, P. N. A General Approach to Binary and Ternary Hybrid Nanocrystals. *Nano Lett.* **2006**, *6* (4), 875–881.

22. Guchhait, A.; Pal, A. J. Copper-Diffused $AgInS_2$ Ternary Nanocrystals in Hybrid Bulk-Heterojunction Solar Cells: Near-Infrared Active Nanophotovoltaics. *ACS Appl. Mater. Interfaces* **2013**, *5* (10), 4181–4189.

23. Chawla, P.; Singh, S.; Sharma, S. N. An Insight into the Mechanism of Charge-Transfer of Hybrid Polymer:Ternary/Quaternary Chalcopyrite Colloidal Nanocrystals. *Beilstein J. Nanotechnol.* **2014**, *5*, 1235–1244.

24. Liu, C.-Y.; Holman, Z. C.; Kortshagen, U. R. Hybrid Solar Cells from P3HT and Silicon Nanocrystals. *Nano Lett.* **2009**, *9* (1), 449–452.

25. Mitra, S.; Cook, S.; Švrček, V.; Blackley, R. A.; Zhou, W.; Kovač, J.; Cvelbar, U.; Mariotti, D. Improved Optoelectronic Properties of Silicon Nanocrystals/Polymer Nanocomposites by Microplasma-Induced Liquid Chemistry. *J. Phys. Chem. C* **2013**, *117* (44), 23198–23207.

26. Hessel, C. M.; Rasch, M. R.; Hueso, J. L.; Goodfellow, B. W.; Akhavan, V. A.; Puvanakrishnan, P.; Tunnel, J. W.; Korgel, B. A. Alkyl Passivation and Amphiphilic Polymer Coating of Silicon Nanocrystals for Diagnostic Imaging. *Small* **2010**, *6* (18), 2026–2034.

27. Höhlein, I. M. D.; Werz, P. D. L.; Veinot, J. G. C.; Rieger, B. Photoluminescent Silicon Nanocrystal-Polymer Hybrid Materials via Surface Initiated Reversible Addition–Fragmentation Chain Transfer (RAFT) Polymerization. *Nanoscale* **2015**, *7* (17), 7811–7818.

28. Yang, Z.; Dasog, M.; Dobbie, A. R.; Lockwood, R.; Zhi, Y.; Meldrum, A.; Veinot, J. G. C. Highly Luminescent Covalently Linked Silicon Nanocrystal/Polystyrene Hybrid Functional Materials: Synthesis, Properties, and Processability. *Adv. Funct. Mater.* **2014**, *24* (10), 1345–1353.

29. Dung, M. X.; Choi, J.-K.; Jeong, H.-D. Newly Synthesized Silicon Quantum Dot–Polystyrene Nanocomposite Having Thermally Robust Positive Charge Trapping. *ACS Appl. Mater. Interfaces* **2013**, *5* (7), 2400–2409.

30. Choi, J.-K.; Dung, M. X.; Jeong, H.-D. Novel Synthesis of Covalently Linked Silicon Quantum Dot–Polystyrene Hybrid Materials: Silicon Quantum Dot–Polystyrene Polymers of Tunable Refractive Index. *Materials Chemistry and Physics* **2014**, *148* (1–2), 463–472.

31. Sato, K.; Fukata, N.; Hirakuri, K.; Murakami, M.; Shimizu, T.; Yamauchi, Y. Flexible and Transparent Silicon Nanoparticle/Polymer Composites with Stable Luminescence. *Chem. Asian J.* **2010**, *5* (1), 50–55.

32. Yan, S. Electrochemical Cells-New Advances in Fundamental Researches and Applications; Croatia: InTech, **2012**

33. Alsharif, N. H.; Berger, C. E. M.; Varanasi, S. S.; Chao, Y.; Horrocks, B. R.; Datta, H. K. Alkyl-Capped Silicon Nanocrystals Lack Cytotoxicity and Have Enhanced Intracellular Accumulation in Malignant Cells via Cholesterol-Dependent Endocytosis. *Small* **2008**, *5* (2), 221–228.

34. Cheng, X.; Lowe, S. B.; Reece, P. J.; Gooding, J. J. Colloidal Silicon Quantum Dots: From Preparation to the Modification of Self-Assembled Monolayers (SAMs) for Bio-Applications. *Chem. Soc. Rev.* **2014**, *43* (8), 2680–2700.

35. McVey, B. F. P.; Tilley, R. D. Solution Synthesis, Optical Properties, and Bioimaging Applications of Silicon Nanocrystals. *Acc. Chem. Res.* **2014**, *47* (10), 3045–3051.

36. Schnabel, M.; Weiss, C.; Löper, P.; Wilshaw, P. R.; Janz, S. Self-Assembled Silicon Nanocrystal Arrays for Photovoltaics: Self-Assembled Silicon Nanocrystal Arrays for Photovoltaics. *Phys. Status Solidi A* **2015**, *212* (8), 1649–1661.

37. Chandra, S.; Masuda, Y.; Shirahata, N.; Winnik, F. M. Transition-Metal-Doped NIR-Emitting Silicon Nanocrystals. *Angew. Chem. Int.* Ed. **2017**, 56 (22), 6157–6160.

38. Mastronardi, M. L.; Hennrich, F.; Henderson, E. J.; Maier-Flaig, F.; Blum, C.; Reichenbach, J.; Lemmer, U.; Kübel, C.; Wang, D.; Kappes, M. M.; et al. Preparation of Monodisperse Silicon Nanocrystals Using Density Gradient Ultracentrifugation. *J. Am. Chem. Soc.* **2011**, *133* (31), 11928–11931.

39. Maier-Flaig, F.; Rinck, J.; Stephan, M.; Bocksrocker, T.; Bruns, M.; Kübel, C.; Powell, A. K.; Ozin, G. A.; Lemmer, U. Multicolor Silicon Light-Emitting Diodes (SiLEDs). *Nano Lett.* **2013**, *13* (2), 475–480.

40. Dong-Chen, Wang.; Chi, Zhang.; Pan, Zeng.; Wen-jie, Zhou.; Lei, Ma; Hao-Tian, Wang; Zhi-Quan, Zhou; Fei, Hu; Shu-Yu, Zhang; Ming, Lu; Xiang, Wu.An Silicon Nanocrystal Laser,Cornell University. *arXiv* **2017**, *1710.00215*.

41. Švrček, V.; Mariotti, D.; Nagai, T.; Shibata, Y.; Turkevych, I.; Kondo, M. Photovoltaic Applications of Silicon Nanocrystal Based Nanostructures Induced by Nanosecond Laser Fragmentation in Liquid Media. *J. Phys. Chem. C* **2011**, *115* (12), 5084–5093.

42. Gonzalez, C. M.; Iqbal, M.; Dasog, M.; Piercey, D.; Lockwood, R. Detection of High-Energy Compounds Using Photoluminescent Silicon Nanocrystal Based Paper Sensors. *Nanoscale.* **2014***,* 7, 2608-2612.

43. Tamarov, K. P.; Osminkina, L. A.; Zinovyev, S. V.; Maximova, K. A.; Kargina, J. V.; Gongalsky, M. B.; Ryabchikov, Y.; Al-Kattan, A.; Sviridov, A. P.; Sentis, M.; et al. Radio Frequency Radiation-Induced Hyperthermia Using Si Nanoparticle-Based Sensitizers for Mild Cancer Therapy. *Sci Rep* **2015**, *4* (1), 7034.

44. Talapin, D. V.; Lee, J.-S.; Kovalenko, M. V.; Shevchenko, E. V. Prospects of Colloidal Nanocrystals for Electronic and Optoelectronic Applications. *Chem. Rev.* **2010**, *110* (1), 389–458.

45. Michalet, X. Quantum Dots for Live Cells, in Vivo Imaging, and Diagnostics. *Science* **2005**, *307* (5709), 538–544.

46. Gao, X.; Cui, Y.; Levenson, R. M.; Chung, L. W. K.; Nie, S. In Vivo Cancer Targeting and Imaging with Semiconductor Quantum Dots. *Nat Biotechnol* **2004**, *22* (8), 969–976.

47. Kirchner, C.; Liedl, T.; Kudera, S.; Pellegrino, T.; Muñoz Javier, A.; Gaub, H. E.; Stölzle, S.; Fertig, N.; Parak, W. J. Cytotoxicity of Colloidal CdSe and CdSe/ZnS Nanoparticles. *Nano Lett.* **2005**, *5* (2), 331–338.

48. Basabe-Desmonts, L.; Reinhoudt, D. N.; Crego-Calama, M. Design of Fluorescent Materials for Chemical Sensing. *Chem. Soc. Rev.* **2007**, *36* (6), 993.

49. Dasog, M.; Kehrle, J.; Rieger, B.; Veinot, J. G. C. Silicon Nanocrystals and Silicon-Polymer Hybrids: Synthesis, Surface Engineering, and Applications. *Angew. Chem. Int. Ed.* **2016**, *55* (7), 2322–2339.

50. Meinardi, F.; Ehrenberg, S.; Dhamo, L.; Carulli, F.; Mauri, M.; Bruni, F.; Simonutti, R.; Kortshagen, U.; Brovelli, S. Highly Efficient Luminescent Solar Concentrators Based on Earth-Abundant Indirect-Bandgap Silicon Quantum Dots. *Nature Photon* **2017**, *11* (3), 177–185.

51. Marinins, A.; Zandi Shafagh, R.; van der Wijngaart, W.; Haraldsson, T.; Linnros, J.; Veinot, J. G. C.; Popov, S.; Sychugov, I. Light-Converting Polymer/Si Nanocrystal Composites with Stable 60–70% Quantum Efficiency and Their Glass Laminates. *ACS Appl. Mater. Interfaces* **2017**, *9* (36), 30267–30272.

52. Pavesi, L.; Negro, L. D.; Mazzoleni, C.; FranzoÁ, G.; Priolo, F. Optical Gain in Silicon Nanocrystals. **2000**, *408*, 5.

53. Wang, D.-C.; Chen, J.-R.; Li, Y.-L.; Song, S.-C.; Guo, W.-P.; Lu, M. Enhancing Optical Gains in Si Nanocrystals via Hydrogenation and Cerium Ion Doping. *Journal of Applied Physics* **2014**, *116* (4), 043512.

54. Sajjadnejad, M.; Mozafari, A.; Omidvar, H.; Javanbakht, M. Preparation and Corrosion Resistance of Pulse Electrodeposited Zn and Zn–SiC Nanocomposite Coatings. *Applied Surface Science* **2014**, *300*, 1–7.

CHAPTER 2. EXPERIMENTAL METHODS

2.1. Quantum yield and PL peak characterization

The quantum yield (QY) was measured by placing a sample in an integrating sphere and exciting the sample with a laser (typically 375 nm). First, the baseline (*e.g.*, 1 mL of 5:1 mesitylene:1-dodecene), which represents the suspending medium used with colloidal silicon nanocrystals (SiNCs), was introduced into the integrating sphere. Then, a vial with 1 mL of colloidal SiNC, passivated/dispersed in 5:1 mesitylene:1-dodecene, was introduced into the integrating sphere. This procedure produced the two curves shown in **Figure 2.1a**, where the dashed curve represents the baseline spectrum and the red curve represents the SiNC spectrum. In **Figure 2.1b**, a sample with an 826 nm PL peak is used as an example to demonstrate how the method works. After the absorption and emission spectra for the baseline and the SiNCs were recorded, the baseline spectrum was subtracted from the SiNC spectrum and then multiplied by the instrument calibration curve to produce the result shown in **Figure 2.1a**. The result is a spectrum with a reversed absorption peak and a normal emission peak. Hence, the QY can be determined using **Eq. 2.1**.[1]

$$QY = \frac{the\ area\ of\ the\ emission\ peak}{the\ area\ of\ the\ absorption\ peak.} \text{ x 100 (\%, without units)} \quad (2.1)$$

In other words, the amount of light emitted from the nanocrystal sample (the area under the emitted peak) divided by the amount of light absorbed by the nanocrystal sample (the area under the absorption peak) times 100 gives us the QY measured in percent. **Figure 2.2a** illustrates the QY setup used in this study. **Figures 2.2b-2.2d** show photo images of the components used to measure QY.

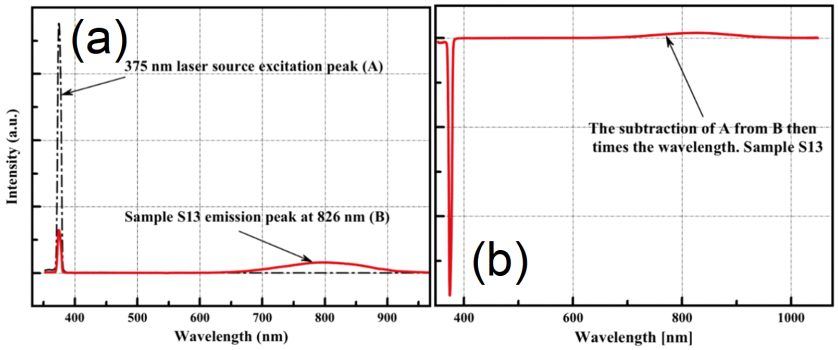

Figure 2.1: (a) Spectra of the baseline and sample. (b) Subtraction of spectrum A (baseline) from spectrum B (specimen).

After performing the QY measurements, the PL peak for the emission is determined. This peak is obtained by fitting a small window of the emission with a zero-background Gaussian function in order to determine the wavelength corresponding to peak emission intensity. The fitting process is illustrated in **Figure 2.3**.

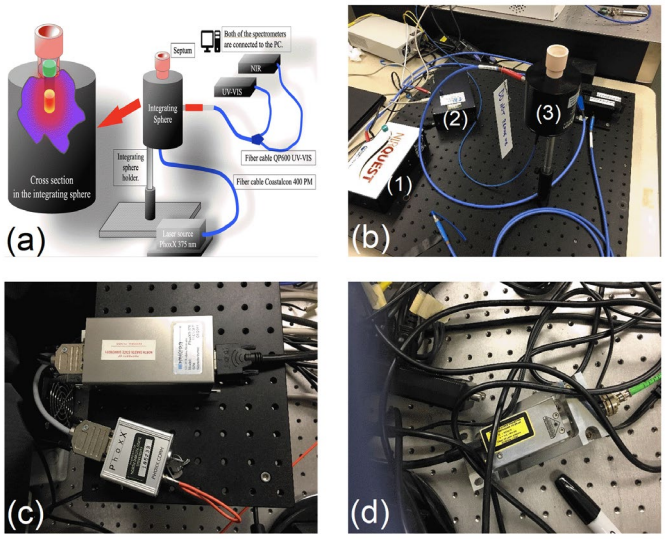

Figure 2.2: (a) Schematic diagram illustrates the QY setup used for the PL-QY characterization. (b) A photo image for the real quantum yield setup used for the measurements (1- NIR spectrometer, 2- UV-VIS spectrometer, and 3- Integrating sphere). (c) The laser power unit of PhoxX laser 375nm. (d) The laser-head unit of the PhoxX laser.

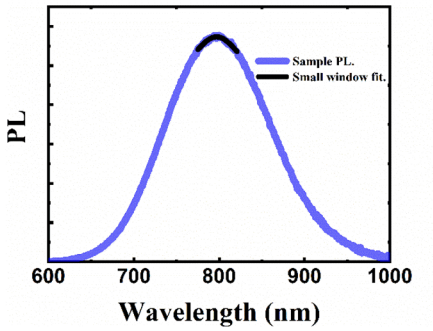

Figure 2.3: The fitting of the emission peak to obtain the PL peak.

2.2. Lifetime measurements

A silicon-nanocrystal (SiNC) emitting PL indicates that electrons and holes are undergoing radiative recombination. Therefore, the time required for the electron to radiatively recombine with the hole is defined as the lifetime.[1] In SiNCs, there are at least two pathways for recombination: the first is very fast, and it needs only nanoseconds to occur; it occurs in the blue part of the spectrum and has to do with the SiNC surface. The second is much slower, and is on the order of microseconds; it represents recombination across the fundamental band gap and occurs mostly in the red to near infrared.

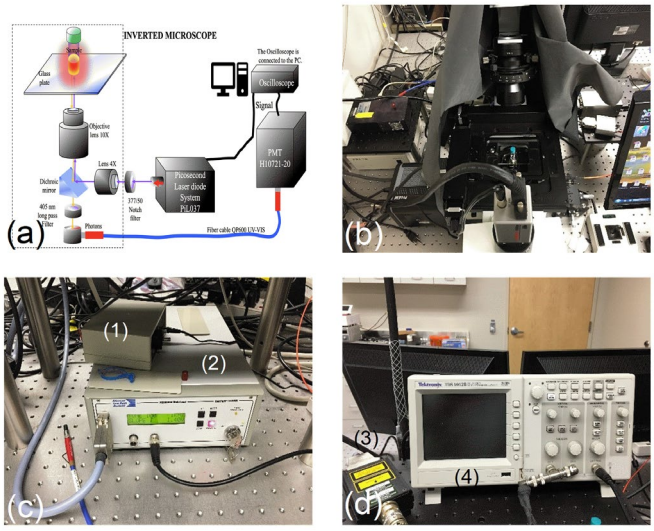

Figure 2.4: (a) Schematic diagram of the lifetime measurement setup. (b) Inverted microscope that is used for the lifetime measurements (OLYMPUS IX 71 inverted microscope). (c) The control unit for the PiL037 picosecond laser diode system and the PMT container (1- PMT and 2- Control unit). (d) The oscilloscope (used to read the PMT signal) and the laser system's head (3- Laser head and 4- Oscilloscope).

Therefore, each recorded pulse represents the detection of an individual photon and, at the same time, illustrates the light intensity at the input. In the present setup, a photomultiplier tube (PMT) is used to detect the photons (**Figure 2.4a**) through the optical fiber and convert them to an electronic pulse that can be read by the oscilloscope. **Figures 2.4b-2.4d** show photo images of the setup to measure the lifetime. A PMT can produce photoelectrons by using the principle of the secondary-electron emission effect, as shown in **Figure 2.5**. The emission photon is received, and then, the photoelectrons are multiplied via the secondary-electron emission effect in order to achieve high-gain amplification.

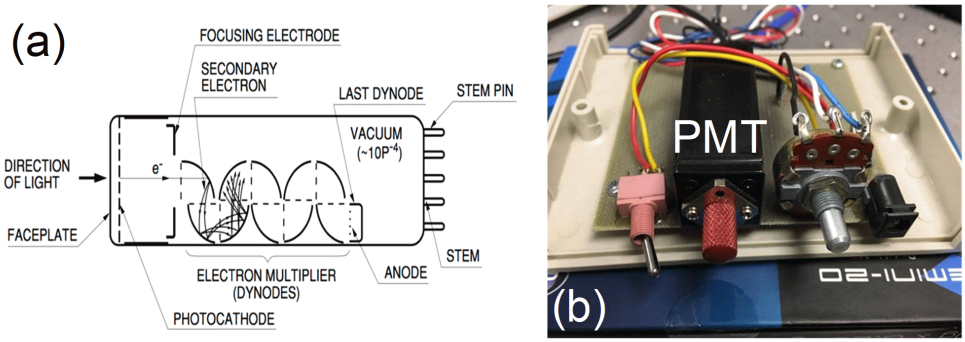

Figure 2.5: (a) The main parts of the photomultiplier tube (PMT). Taken from Ref. [2] (b) The PMT used to characterize the lifetime of the studied samples (H10721-20, Hamamatsu, Bridgewater Township, NJ).

The frequency of the laser source and the gain of the PMT were changed at the beginning of the experiment to ensure optimized signal. The fast and slow relaxations were analyzed by fitting the data to a double stretched exponential (**Eq. 2.2**). An example is shown in **Figure 2.6**.

$$I(t) = A_1 \, e^{\left[-\frac{t}{\tau_1}\right]^{\alpha_1}} + A_2 \, e^{\left[-\frac{t}{\tau_2}\right]^{\alpha_2}} \tag{2.2}$$

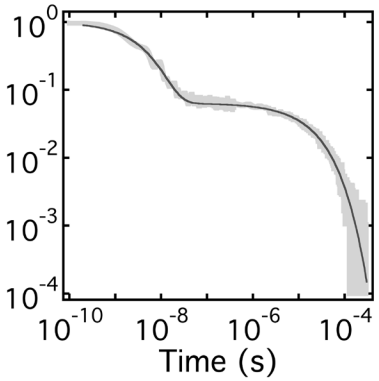

Figure 2.6: Representative PL intensity decay with the fitting curve.

2.3. Transmission electron microscopy (TEM) size characterization

High-resolution transmission electron microscopy (HRTEM) characterization was performed using a JEOL JEM-2100 HRTEM operated at 200 kV. The TEM grid was prepared by collecting a thin layer of concentrated silicon nanocrystals (SiNCs) cast from organic solvent on a Langmuir trough of diethylene glycol, and then dipping the grid in de-ionized (DI) water.

The grid was kept under a vacuum for 48 h to remove excess solvent. The particles were measured and counted using ImageJ software, and the polydispersity index (PDI) was calculated using the following formulas.[3]

$$D_N = \frac{\Sigma_i p_i d_i}{\Sigma_i p_i} \tag{2.3}$$

$$D_W = \frac{\Sigma_i p_i d_i^2}{\Sigma_i p_i d_i} \tag{2.4}$$

$$PDI = \frac{D_W}{D_N} \tag{2.5}$$

where D_N = the number average diameter, D_W = the weight average diameter, PDI = the polydispersity index, and d_i = the diameter of the SiNCs.

2.4. The raw material used to synthesize SiNC/ off-stoichiometric thiol-ene (OSTE)

The SiNC/OSTE nanocomposite samples were prepared with the cascade polymerization reaction of the OSTE polymer and 1-dodecene-terminated SiNCs.[1] The OSTE polymer was formed from thiol monomers, allyl monomers, and an initiator, which undergo a click-chemistry reaction. These chemicals were purchased from Sigma Aldrich and had purity greater than 95%. The 1-dodecene-terminated SiNCs were synthesized with cyclohexasilane (Si_6H_{12}) using a cold plasma reactor.[4] **Table 2.1** shows the surface passivation and rough size of the SiNC samples used for this study that were exposed to the lab atmosphere. **Table 2.2** shows the surface passivation and rough size of the second group of SiNC samples utilized for this study that were never exposed to the lab atmosphere. Nanocrystal size in these tables is estimated from the position of the PL peak using an experimental metric derived for size-purified SiNCs.[4]

Table 2.1: Sample labels, surface ligands, and the approximate size of lab exposed SiNC samples.

Sample	Surface ligands	2R (nm)
R56D	Hexene:1-dodecene 0.0:1.0	2.86
R59D	Hexene:1-dodecene 0.0:1.0	3.10
R49D	Hexene:1-dodecene 0.0:1.0	3.13
R109D	Hexene:1-dodecene 0.0:1.0	3.33
R112-2D	Hexene:1-dodecene 0.0:1.0	4.66
R75D	Hexene:1-dodecene 0.0:1.0	4.85

Table 2.2: Sample labels, surface ligands, and the approximate size of unexposed SiNC samples.

Sample	Surface ligands	2R (nm)
R106HD	Hexene:1-dodecene 0.5:0.5	2.81
R55D	Hexene:1-dodecene 0.0:1.0	2.91
R67D	Hexene:1-dodecene 0.0:1.0	3.74
R68D	Hexene:1-dodecene 0.0:1.0	4.32
R78HD	Hexene:1-dodecene 0.5:0.5	4.79
R74D	Hexene:1-dodecene 0.0:1.0	5.06
R24D	Hexene:1-dodecene 0.0:1.0	5.41

2.5. Preparation methods used to create SiNC/OSTE nanocomposites

In general, the process was divided into two main stages. In stage one, the SiNC/mesitylene was concentrated to achieve highly concentrated SiNC/1-dodecene/mesitylene through evaporation under a N_2 atmosphere. Stage two prepared the nanocomposite, and was divided into four main methods described below.

2.5.1. First preparation method

The first preparation method used the following steps:[5,6]

a. Mix the initiator with allyl monomers.

b. Add the thiol monomers to the mixture from step (a).

c. Add the concentrated SiNC/mesitylene colloid to the mixture from step (b).

d. Mix and sonicate the resulting colloid from step (c) four times for 2 min each.

e. Cure the mixture using a 365-nm LED light immediately after the mixing process.

f. The baseline pure OSTE sample was made using steps (a) through (e) without adding SiNCs.

Figure 2.7 shows the steps to prepare the SiNC/OSTE nanocomposite sample using the first preparation method.

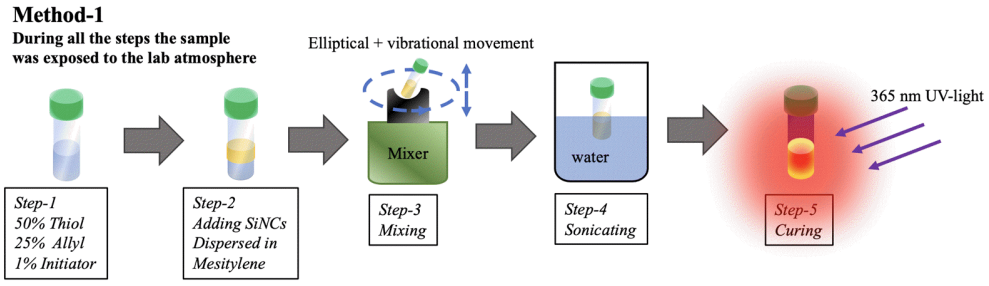

Figure 2.7: The steps of synthesizing SiNC/OSTE nanocomposites (first preparation method). The parent was exposed to the lab atmosphere.

2.5.2. The second preparation method

The second preparation method (**Figure 2.8**) added toluene for step 1 and followed the same steps that were completed with the first method. Then, the mixture was concentrated for 20 hours before the nanocomposite sample was cured. The same steps were applied to produce the baseline. The descriptions are shortened for the following steps:

a. Add the initiator to the monomers before starting the polymerization reaction.

b. Stir the mixture thoroughly.

c. Sonicate the mixture four times for 2 min each.

d. Add the concentrated SiNC/mesitylene colloid, and stir the mixture until all components are homogeneously mixed.

e. The colloid is concentrated so that the mixture is as close to the original viscosity as possible. It takes around 20 hours to remove the extra toluene. The resulting colloid is cured using a 365 nm LED immediately after the evaporation process.

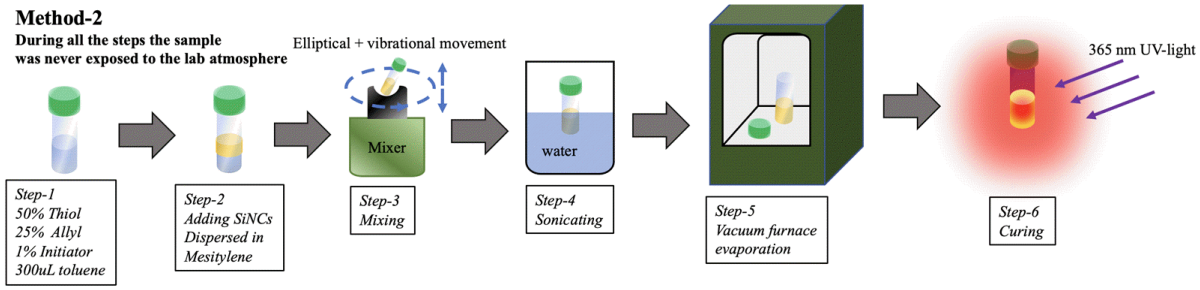

Figure 2.8: The steps of synthesizing the SiNC/OSTE nanocomposites (second preparation method). The parent was exposed to the lab atmosphere.

2.5.3. The third preparation method

The third preparation method is similar to the first method, but all the steps are performed in a glove box. Furthermore, an integrating sphere with a 375 nm excitation source was used to cure the mixture instead of the 365 nm LED. The following steps describe how the third preparation method works:

a. Mix 0.04 g initiator with 1 g allyl monomers.

b. Add 2 g thiol monomers to the mixture from step (a).

c. Add 140 µL concentrated SiNC/mesitylene colloid, which was concentrated in a glove box, to the mixture from step (b).

d. Seal the colloid from step (c) in a 20 mL vial and then thoroughly stir. Then, sonicate the mixture four times for 2 min each.

e. After 6 hours, cure the mixture using a 375 nm PhoxX laser to complete the preparation process.

f. The baseline reference sample was made using steps (a) through (e), without adding SiNCs.

Figure 2.9 shows the steps to prepare the SiNC/OSTE nanocomposite sample using the third preparation method.

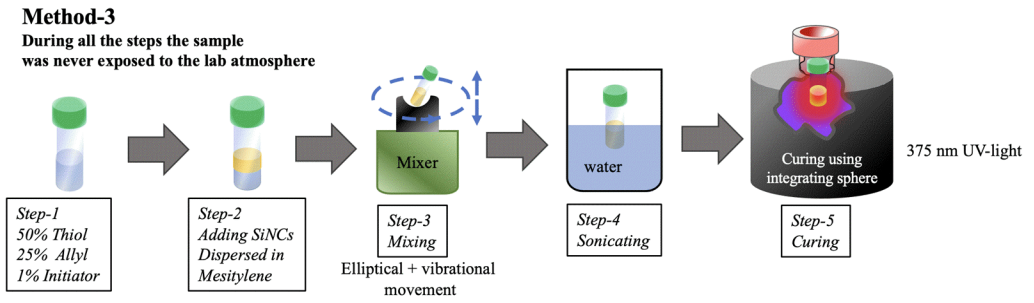

Figure 2.9: The steps of synthesizing the SiNC/OSTE nanocomposites (third preparation method). The parent was never exposed to the lab atmosphere.

2.5.4. The fourth preparation method

The fourth preparation method requires attempting to remove the dissolved O_2 from the raw resin material to prevent SiNCs oxygen exposure and adding toluene to achieve a homogeneous mixture, as shown in **Figure 2.10** step one. This method shields the SiNCs from oxygen during the preparation steps, but the toluene must be completely evaporated.

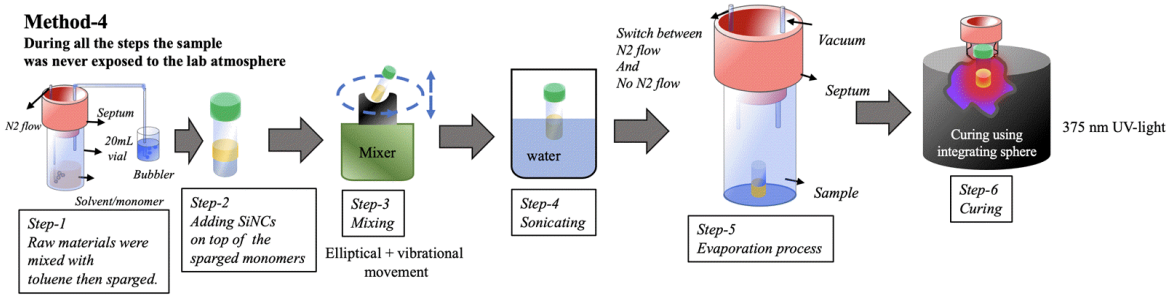

Figure 2.10: The steps of synthesizing the SiNC/OSTE nanocomposites (fourth preparation method). The parent was never exposed to the lab atmosphere.

The steps are summarized below:

a. Sparge the organic solvents (mesitylene:1-dodecene and toluene). This step is always done for every colloidal SiNC suspension made in our lab but was not noted above because it specifically pertains to the resin here.

b. Dissolve the raw materials (thiol, allyl, and initiator) in toluene, separately.

c. Shake each mixture thoroughly, and then, sonicate for 2 min each.

d. Pour each mixture into a Shlenk tube, and seal it with the septum, as shown in **Figure 2.10**, to start the sparging process for the raw materials. This step takes around 2 hours. The same idea is applied to each raw material. Toluene is used to avoid the high viscosity of the thiol and allyl monomers.

e. Mix the monomers and SiNCs thoroughly for 2 min, and then, sonicate the mixture for another 2 min. The colloid is less viscous now because of the toluene content.

f. Concentrate the colloid so that it is as close to the original viscosity as possible and has the required amounts of each raw-material component. To remove the extra toluene, this process takes around 20 hours in a vacuum.

g. Cure the resultant colloid using a 375 nm PhoxX laser immediately after the evaporation process finishes.

2.5.5. The approved preparation method for preparing OSTE Polymer Composites

This is the approach that gave the most consistent results in terms of low composite turbidity and good composite QY. The nanocomposites were prepared using a number of different approaches as mentioned above, but the approach utilized for the samples discussed in Chapters 7, 8, and 9 (**Figure 2.11**) was as follows. A parent colloidal SiNC suspension (around 1 ml at 2 mg/ml SiNCs in mesitylene) was concentrated under vacuum down to a volume of 120 µl consisting predominantly of SiNCs and 1-dodecene, where the latter is both bound and free.

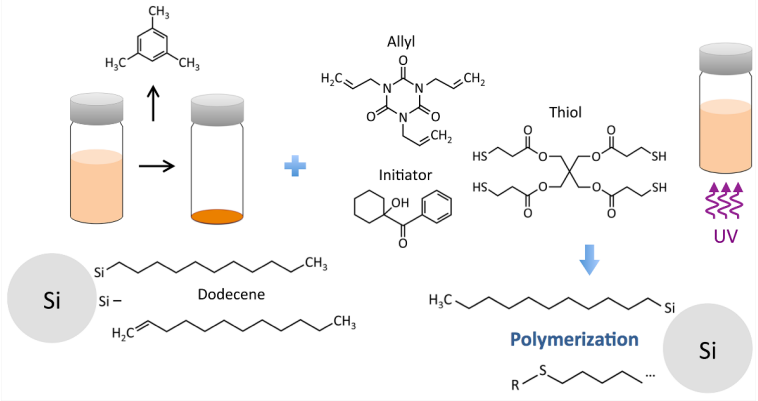

Figure 2.11: Colloidal SiNCs passivated with 1-dodecene and suspended in mesitylene are dried under vacuum and the solvent is replaced with the OSTE resin mixture. Polymerization of the matrix and residual ligand is then activated by exposure to UV light. All samples were shielded from exposure to air and were processed in a nitrogen atmosphere.

Separately, 40 µL of initiator was mixed with 1 ml of allyl, which was then mixed with 2 ml of thiol resin. The final thiol:(olefin + allyl) molar ratio is approximately 1.30:1.00 with an olefin:allyl molar ratio of about 1:200. The SiNCs were then mixed into the resin in a clean vial identical to those used to measure the QY of the colloid, first by vortexing and then by sonicating. After the sample became clear, photo-polymerization was initiated by placing the vial in the integrating sphere under UV laser illumination (4 mW at 375 nm) for several minutes. SiNC-free reference vials were prepared as described above with the SiNC volume replaced by an equivalent volume (140 µl) of 5:1 mesitylene:1-dodecene. Excess mesitylene acts as plasticizer in the composites, while excess 1-dodecene reacts with the OSTE components to become part of the polymer matrix.

2.6. UV-light treatment for SiNC/OSTE composite

The process of curing is considered an essential step for achieving desirable optical specifications. Two different curing methods were used in the current study. In one, the sample was simply exposed to a 365 nm LED on a lab bench. The second method uses an integrating sphere to distribute the UV light equally across the sample surface. When UV light shines on the

sample from all directions, the photochemical reactions responsible for creating the nanocomposites are homogeneous. **Figure 2.12a and b** show how the integrating sphere is used to perform the curing process.

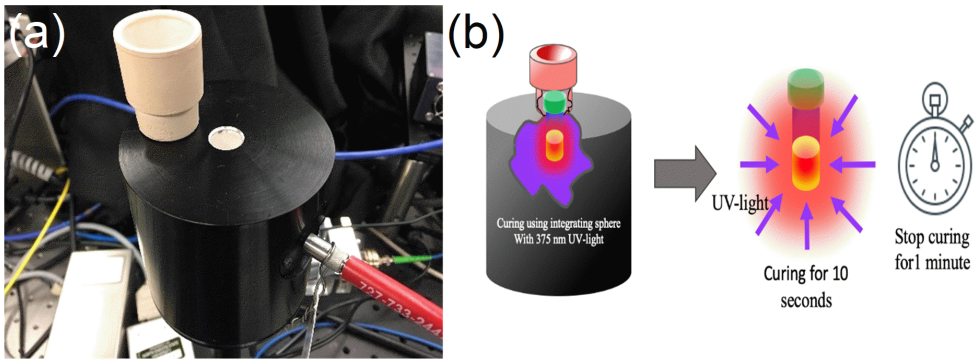

Figure 2.12: (a) The integrating sphere used for the curing process. (b) A digram mimics the real curing process.

Qualities that may interfere with the photophysical measurements are distortion in the upper surface of the nanocomposite sample as in **Figure 2.13c**, longitudinal bubbles as in **Figure 2.13d**, surface vortices and small bubbles as in **Figure 2.13e**, or flat cracks as in **Figure 2.13f**. However, using the integrating sphere for curing is very successful. Examples of nanocomposites that were cured using integrating sphere, while never being exposed to the lab atmosphere during the entire process, are shown in **Figure 2.14**.

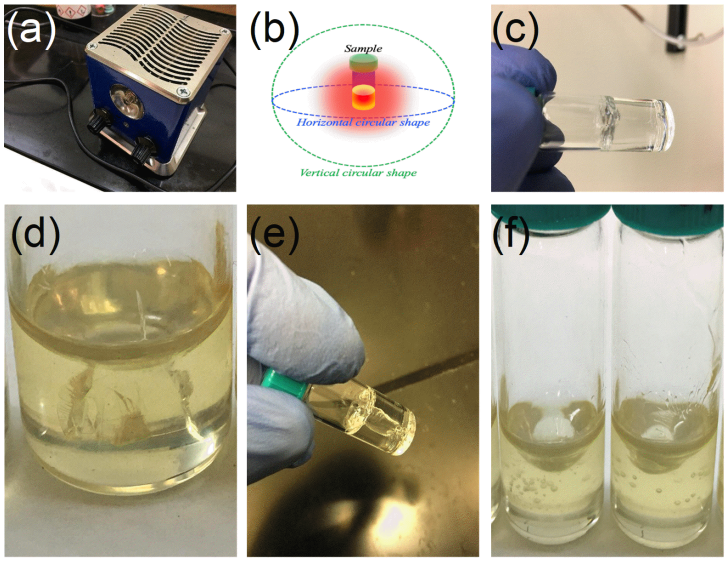

Figure 2.13: UV-light source (365 nm) (a) and process (b) of manually curing nanocomposite samples and common defects with manual curing small bubbles (c), longitudinal bubbles (d), upper-surface distortion (e), and flat cracks (f).

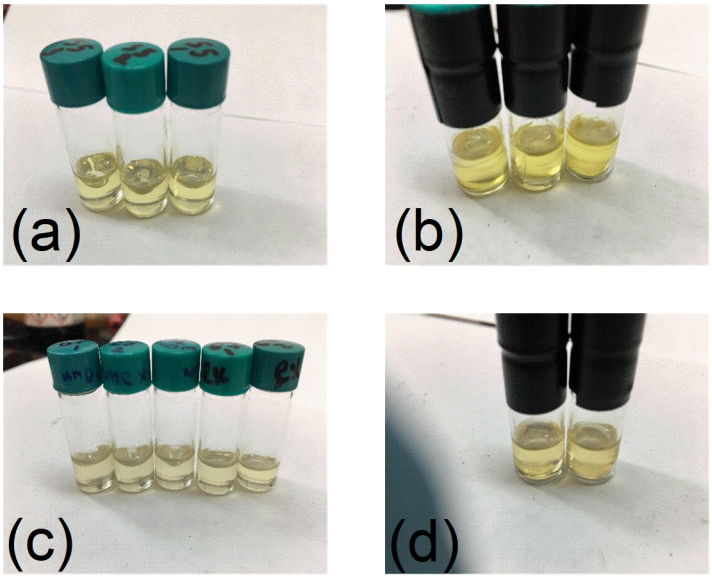

Figure 2.14: Examples of samples that were cured according to the integrating sphere technique. The nanocomposite samples were prepared with the same SiNC content (70 µL pre 1.5g monomers), and all parents have the same concentration of SiNCs (around 3 mg/mL). (a) Prepared from R55D / Preparation method 3 used / Cured for 170 s. (b) Prepared from R106HD / Preparation method 4 / used Cured for 170 s. (c) Prepared from R67D / Preparation method 3 used / Cured for 170 s. (d) Prepared from R68D / Preparation method 4 used / Cured for 170 s.

One advantage of the integrating sphere method is that we do not need to make more than one copy of the nanocomposite sample because this technique reduces the appearance of defects. **Figure 2.15** represents a group of baselines, which were prepared using different methods and different curing techniques.

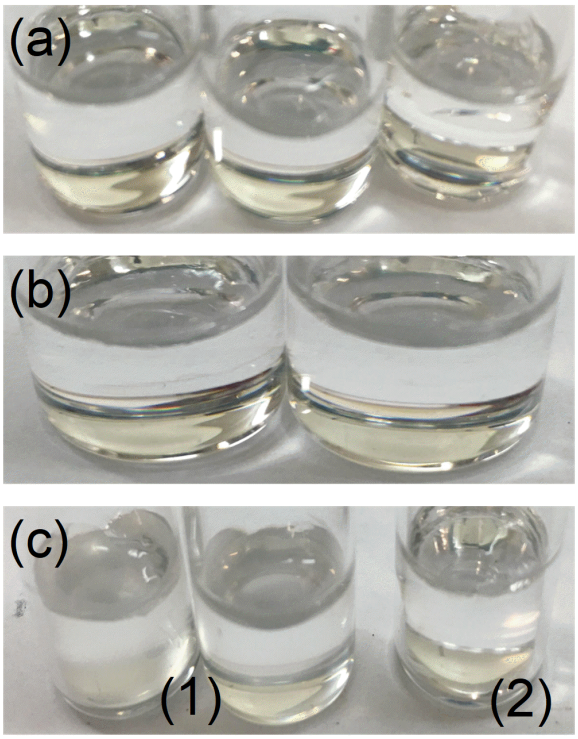

Figure 2.15: A group of OSTE baselines prepared using different methods. (a) Prepared using method 1/Cured using the first technique / Cured for 60 s. (b) Prepared using method 3/ Cured using the second technique / Cured for 170 s. (c) 1- Prepared using method 4 / Cured using the second technique / Cured for 170 s and 2- Prepared using method 2 / Cured using the first technique / Cured for 60 s.

2.7. Photoluminescence measurements under temperature control

To measure the PL under cryogenic conditions, a Linkham Biological Cryo-Stage (BCS196) was used. Samples for cryogenic measurement were prepared as described above but cured as a droplet on a glass cover slip by exposure to an external UV light source.

2.8. Bibliography

1. Lorenzo, P. and Rasit, T. Silicon Nanocrystals, Mörlenbach: Wiley-VCH Verlag, **2010**.

2. https://www.hamamatsu.com

3. Nematollahzadeh, A.; Abdekhodaie, J. M; Shojaei, A., Submicron Nanoporous Polyacrylamide Beads with Tunable Size for Verapamil Imprinting. *J. Appl. Polym. Sci.* **2012**, 125,189–199

4. Pringle, T. A.; Hunter, K. I.; Brumberg, A .; Anderson, K.; Fagan, J. A.; Thomas, S. A.; Petersen, R. J.; Sefannaser, M.; Han, Y.; Brown, S. L.; Kilin, D. S.; Schaller, R. D.; Kortshagen, U. R.; Boudjouk, P.; Hobbie, E. K., Bright Silicon Nanocrystals from a Liquid Precursor: Quasi-Direct Recombination with High Quantum Yield. *ACS Nano* **2020**, *14*, 3858–3867.

5. Marinins, A.; Zandi Shafagh, R.; van der Wijngaart, W.; Haraldsson, T.; Linnros, J.; Veinot, J. G. C.; Popov, S.; Sychugov, I. Light-Converting Polymer/Si Nanocrystal Composites with Stable 60–70% Quantum Efficiency and Their Glass Laminates. *ACS Appl. Mater. Interfaces* **2017**, *9* (36), 30267–30272.

6. Lowe, A. B. Thiol–Ene "Click" Reactions and Recent Applications in Polymer and Materials Synthesis: A First Update. *Polym. Chem.* **2014**, *5* (17), 4820–4870.

CHAPTER 3. HIGH QUANTUM YIELD FROM SILICON NANOCRYSTALS SYNTHESIZED FROM LIQUID PRECURSOR USING COLD PLASMA REACTOR

3.1. Introduction

The potential applications of quantum dots have become one of the most researched topics in the current field of nanotechnology. Biology, computing, photovoltaic devices, and light-emitting devices are all examples of these potential fields of use. The size-tunable photoluminescence is a unique feature of quantum dots. Quantum dots such as CdSe, CdS, and CdTe show high fluorescence, yet they are potentially toxic in the environment. Consequently, developing non-toxic quantum dots, which can be used safely in a broad range of applications, is essential for the future.

Silicon nanocrystals (SiNCs) have attracted attention as next-generation quantum dots. SiNCs are a non-toxic material made from an earth-abundant element. The most crucial property of SiNCs is that they have photoluminescence (PL) caused by radiative recombination of excitons within the SiNC.[1] Furthermore, the color of the emitted light from SiNCs is tuned by changing the size of the nanocrystal.[2] The size-dependent optical properties of SiNCs represent an essential feature for many applications, such as photovoltaic devices, electroluminescent displays, cancer cell visualization, and light-emitting devices.

SiNCs have been synthesized using a variety of approaches, including chemical vapor deposition, ion-implantation, and laser ablation.[3] However, all the mentioned techniques produce small amounts of SiNCs, which can affect specific applications. Therefore, it is necessary to develop a new preparation technique to ensure both higher mass-production and better photophysical properties.

To overcome the described difficulty, our group focused on non-thermal plasma reaction as a technique to synthesize SiNCs using cyclohexasilane (Si_6H_{12}) as a precursor. The non-thermal plasma reaction offers excellent productivity and can control both the particle size and surface structure of the SiNCs.[4]

In this chapter, we study the photophysical properties of SiNCs that are synthesized from Si_6H_{12} using a cold plasma reaction and capped with 1-dodecene. The QY, lifetime, and PL peak of SiNCs are strongly related to surface termination and nanocrystal size, and these variables can be used to control the photophysical properties of SiNCs. In this section, we investigate the relationships between all of these variables and how they relate to the method of preparation.

3.2. Results and discussion

The silicon nanocrystals (SiNCs) used in this study were synthesized with cyclohexasilane (Si_6H_{12}) using a non-thermal plasma reactor and subsequently passivated with 1-dodecene through thermal hydrosilylation in a mesitylene solution. All the photoluminescence (PL) measurements in this section were performed on samples that were never exposed to air. A glove box was used to conduct the preparation steps under a nitrogen atmosphere. During the PL measurements, the samples were kept in sealed 2 mL vials to prevent exposure to ambient oxygen and water.

Figures 3.1a and 3.1c show an example of a TEM image and size distribution histogram of one of the polydisperse SiNC samples (900 nm PL peak), which was passivated with 1-dodecene. In **Figure 3.1b**, the high crystallinity is evident through the featured lattice fringes, which have a size of 0.3 nm, and the lattice fringes are in good agreement with the (111) crystalline plane of silicon.[5] The average size of the mentioned sample was determined by fitting the size distribution in **Figure 3.1c** with a Gaussian function. The average size is 4.3 nm, and it

corresponds to the peak of the Gaussian function. The sample had a polydispersity index (PDI) close to 1, which indicates a quasi-uniform particle size distribution.

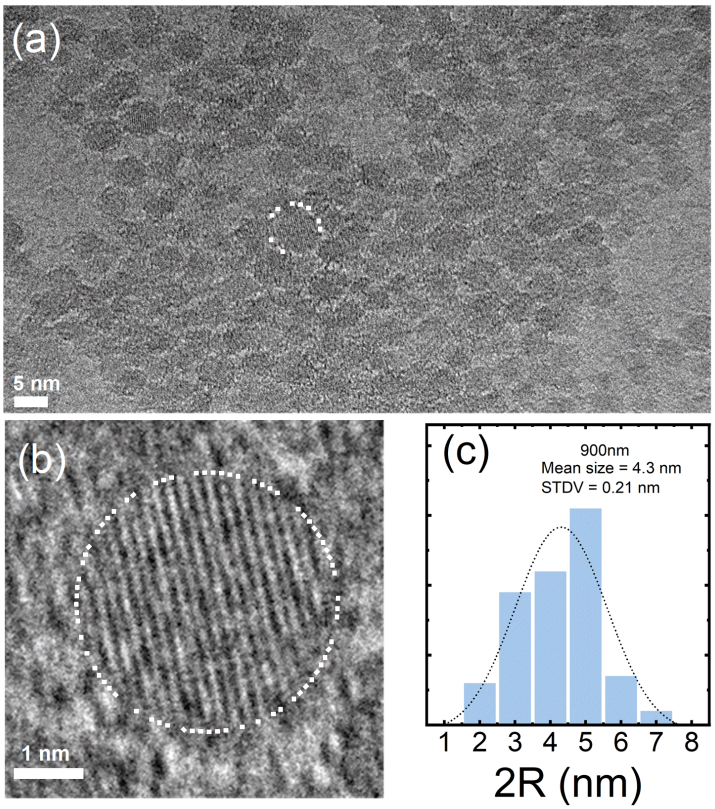

Figure 3.1: (a) TEM image of SiNCs for the sample with 900 nm PL peak. (b) Single SiNC magnified from image (a). The yellow circle indicates the borders of the SiNC. (c) Size distribution histogram extracted from TEM data.

Table 3.1. presents PL-QY measurements for six selected samples with a PL peak that varies from 716 to 923 nm. Samples with PL peaks of 718 nm, 806 nm, and 870 nm had a second PL-QY characterization after 75 days. Both measurements still have the same PL peak, as shown in **Table 3.1,** with a small difference in QY. This difference does not indicate any degradation because the QY became slightly higher after more than two months. This result could be related to self-passivation since the samples were exposed to both excitation sources during the PL-QY measurements and visible light during storage in the glove box.[6,7] In contrast,

samples with PL peaks 859 nm, 883 nm, and 923 nm did not have any noticeable change in either their QY or PL peak as shown in **Table 3.1**.

Table 3.1: Comparing the photophysical properties of a group of SiNCs samples, having sizes from 2.92 nm to 5.25 nm, before and after 75 days.

Sample size (nm)	QY (%)				PL peak (nm)			
	QY_a	QY_b	Error	ΔQY	PLP_a	PLP_b	Error	ΔPLP
2.92	29	31	±5.0	2	718	718	±0.2	0
3.63	48	52	±5.0	4	806	806	±0.2	0
4.22	26	27	±5.0	1	859	859	±0.2	0
4.37	50	54	±5.0	4	870	871	±0.2	0
465	52	52	±5.0	0	883	883	±0.2	1
5.25	39	39	±5.0	0	923	923	±0.2	0

Note. QY_a = First measurement of QY, QY_b = Second measurement of QY after 75 days.

The PL of the colloidal SiNCs samples with PL peaks of 930 nm and 750 nm, and passivated with 100% 1-dodecene, were studied in both cases before and after exposure to the lab atmosphere. The PL measurements were first obtained with an unexposed sample vial for both colloidal samples. Then the sample vials were opened for an hour and recapped. The sample with a 930 nm peak was kept for 300 days before re-measuring the PL for the second time. However, a sample with PL peak 750 nm was kept in the lab atmosphere for one day (24 hours) with a sealed cap. The PL for both samples shown in **Figure 3.2**. The ratio in PL was calculated by dividing the PL of the unexposed sample by the PL of the exposed sample. It is clear that the sample with 930 nm PL peak has blueshifted, and the sample with 750nm PL peak has redshifted. What is the origin of the two shifts when the sample is exposed to the lab atmosphere? To probe this behavior, quantum yield was measured for both samples. The 930 nm sample experienced a drop-in quantum yield from 30.8 to 12.7 %, while the sample with 750 nm dropped from 34.4 to 27.2 %. In both cases, quantum yield drops to lower values, but the sample with 930 nm PL peak has the largest quantum yield drop. The drop-in quantum yield tells us that the SiNCs in both samples are degraded.

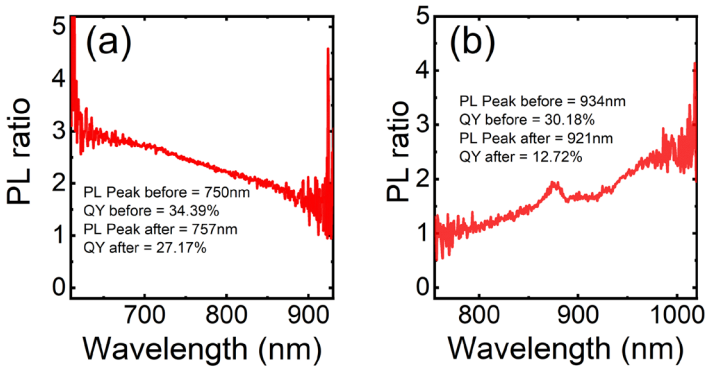

Figure 3.2: (a) & (b) PL ratio of two different samples measured in both cases: before and after exposure to the lab atmosphere. The PL peak and QY are labeled on the graphs.

The sample with 750 nm PL peak experienced a redshift, as shown in **Figure 3.2a**. Typically, increasing NC size leads to a redshift in the photoluminescence peak (PL peak),[8, 9] while the oxidation process is associated with blueshifted PL, as in **Figure 3.2b**.

The PL spectral distribution of 19 selected samples, with PL peaks from 716 to 908 nm, was studied. The colloidal SiNCs samples gave a clear picture of how the polydisperse samples differ in size (**Figure 3.3a**), and it represents a typical distribution. Compared to PL, absorption appears to only weakly depend on the SiNCs size (**Figure 3.3b**) and, mainly, the absorption occurs at the direct optical transition of silicon.[10,11] The PL linewidth increases with decreasing PL peak, or decreasing SiNC size.

The linewidth of the studied polydisperse samples ranges from 0.22 to 0.32 eV with 908 nm and 753 nm PL peaks, respectively, where the narrowest PL spectrum has a linewidth of about 0.22 eV with a 908 nm PL peak. This behavior is strongly related to both size polydispersity and the indirect nature of the SiNC bandgap.[12] **Figure 3.3c** shows the behavior of the linewidth (FWHM) versus PL peak.

Figure 3.3d shows the PL lifetime as a function of PL peak. The SiNC samples exhibit measured lifetimes in the range of 30 to 200 µs, which increases with increasing the PL peak.

The lifetime trend is consistent with previously reported SiNC lifetime study.[13,14] Since the PL of the SiNCs arises from quantum-confined excitons, our lifetime data are only resolvable below around 950 nm PL peak. The lifetime increases strongly with PL peak or nanocrystal size up to relatively high PL peak values. As can be seen from **Figure 3.3d**, the lifetime increases exponentially with increasing PL peak energy, where the black curve represents an exponential function.[15]

Figure 3.3e shows the PL quantum yield (QY) data versus PL peak, which was measured using a baseline of mesitylene:1-dodecene (5:1) solution. The results show that the QY of the polydisperse SiNCs smoothly increases from a minimum of 13 % for sample R87D (containing on average the smallest emitting SiNCs among the studied group) to a maximum value of around 60 % near an emission peak of 850 nm containing medium sized SiNCs.

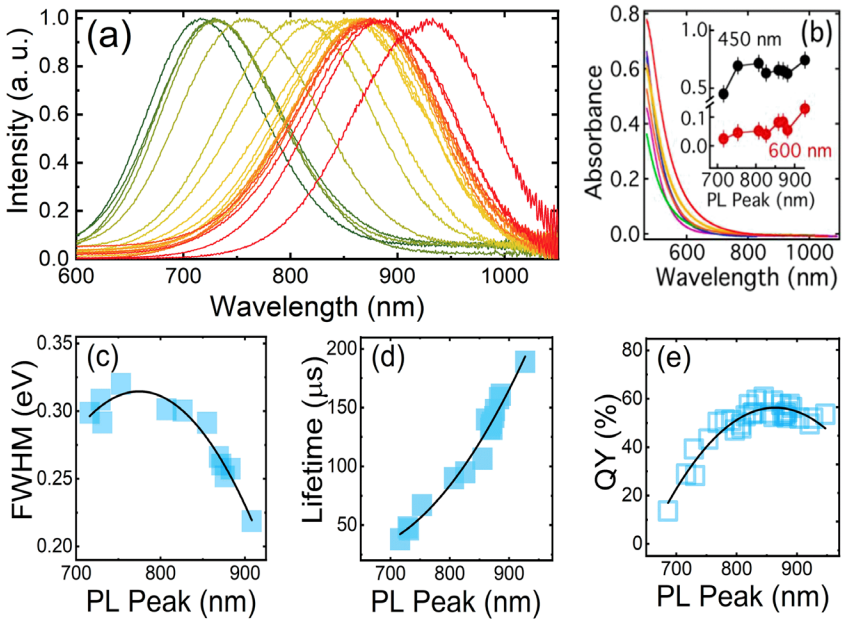

Figure 3.3: (a) Photoluminescence spectra of SiNC samples used in this study. The SiNCs are dispersed in mesitylene:1-dodecene (5:1) and excited at 375 nm after functionalization with 1-dodecene. (b) Normalized absorption spectra for some of the samples shown in figure 3.3a. The inset shows the absorption at 600nm (red) and 450nm (black) as a function of PL peak wavelength. (c) FWHM versus PL peak, where the fit line represents the trend of the FWHM. (d) Slow relaxation time plotted against PL peak, where the fit line represents the trend of the lifetime. (e) QY plotted against PL peak, where the fit line represents the trend of the QY.

The QY values start to drop to around 40 % close to 950 nm, which contains the largest SiNCs among the studied samples considered here. These QY values are considered comparable to or better than the best values that have been reported in the literature.[16,17] The behavior of the QY curve, in general, follows the trend of the black curve in **Figure 3.3e**. One possible explanation is that the QY is determined from the competition between the radiative recombination rate induced by quantum confinement and the increase in the number of surface defects due to the more significant surface effects in smaller nanocrystals.[12] For larger nanocrystals, the exciton has more room to diffuse, which increases the likelihood of encountering a defect. Consequently, the QY tends to decrease when moving toward either smaller or larger SiNCs around the optimum QY value (PL peak of approximately 850 nm).

3.3. Conclusion

In summary, parent as-passivated SiNC samples show a quasi-uniform particle-size distribution based on TEM, with a size-dependent PL response that is in good agreement with what has been reported in the literature, colloidal suspensions exposed to ambient conditions showed PL degradation, which we attribute oxygen exposure.

3.4. Bibliography

1. Ledoux, G.; Guillois, O.; Porterat, D.; Reynaud, C.; Huisken, F.; Kohn, B.; Paillard, V. Photoluminescence Properties of Silicon Nanocrystals as a Function of Their Size. *Phys. Rev. B* **2000**, *62* (23), 15942–15951.

2. Sato, K.; Tsuji, H.; Hirakuri, K.; Fukata, N.; Yamauchi, Y. Controlled Chemical Etching for Silicon Nanocrystals with Wavelength-Tunable Photoluminescence. *Chem. Commun.* **2009**, No. 25, 3759.

3. Silicon Nanocrystals; Lorenzo, P. and Rasit, T.; Wiley-VCH Verlag, **2010.**

4. Tyczkowski, J. Cold Plasma – A Promising Tool for the Development of Electrochemical Cells. In Electrochemical Cells - New Advances in Fundamental Researches and Applications; Shao, Y., Ed.; InTech, **2012**.

5. Mitra, S.; Švrček, V.; Macias-Montero, M.; Velusamy, T.; Mariotti, D. Temperature-Dependent Photoluminescence of Surface-Engineered Silicon Nanocrystals. *Sci Rep* **2016**, *6* (1), 27727.

6. Fernando A. Reboredo.; Eric Schwegler.; Giulia Galli. Optically Activated Functionalization Reactions in Si Quantum Dots. *J. Am Chem Soc.* ***2003***. 125, 15243-15249.

7. Joel A. Kelly; Amber M. Shukaliak; Michael D. Fleischauer; Jonathan G. C. Veinot. Size-Dependent Reactivity in Hydrosilylation of Silicon Nanocrystals. *J. Am Chem Soc*. **2011**,133, 9564-9571.

8. Belyakov, V. A.; Burdov, V. A.; Lockwood, R.; Meldrum, A. Electron Tunneling in Ensembles of Silicon Nanocrystals. *Bull. Russ. Acad. Sci. Phys.* **2010**, *74* (8), 1080–1082.

9. Nishida, M. Electronic State Calculations of Si Quantum Dots: Oxidation Effects. *Phys. Rev. B* **2004**, *69* (16), 165324.

10. Wen, X.; Zhang, P.; Smith, T. A.; Anthony, R. J.; Kortshagen, U. R.; Yu, P.; Feng, Y.; Shrestha, S.; Coniber, G.; Huang, S. Tunability Limit of Photoluminescence in Colloidal Silicon Nanocrystals. *Sci Rep* **2015**, *5* (1), 12469.

11. Lee, B. G.; Luo, J.-W.; Neale, N. R.; Beard, M. C.; Hiller, D.; Zacharias, M.; Stradins, P.; Zunger, A. Quasi-Direct Optical Transitions in Silicon Nanocrystals with Intensity Exceeding the Bulk. *Nano Lett.* **2016**, *16* (3), 1583–1589.

12. Sychugov, I.; Fucikova, A.; Pevere, F.; Yang, Z.; Veinot, J. G. C.; Linnros, J. Ultranarrow Luminescence Linewidth of Silicon Nanocrystals and Influence of Matrix. *ACS Photonics* **2014**, *1* (10), 998–1005.

13. Sugimoto, H.; Fujii, M.; Imakita, K.; Hayashi, S.; Akamatsu, K. Codoping N- and p-Type Impurities in Colloidal Silicon Nanocrystals: Controlling Luminescence Energy from below Bulk Band Gap to Visible Range. *J. Phys. Chem. C* **2013**, *117* (22), 11850–11857.

14. Mastronardi, M. L.; Maier-Flaig, F.; Faulkner, D.; Henderson, E. J.; Kübel, C.; Lemmer, U.; Ozin, G. A. Size-Dependent Absolute Quantum Yields for Size-Separated Colloidally-Stable Silicon Nanocrystals. *Nano Lett.* **2012**, *12* (1), 337–342.

15. Miller, J. B.; Van Sickle, A. R.; Anthony, R. J.; Kroll, D. M.; Kortshagen, U. R.; Hobbie, E. K. Ensemble Brightening and Enhanced Quantum Yield in Size-Purified Silicon Nanocrystals. *ACS Nano* **2012**, *6* (8), 7389–7396.

16. Mangolini, L.; Thimsen, E.; Kortshagen, U. High-Yield Plasma Synthesis of Luminescent Silicon Nanocrystals. *Nano Lett.* **2005**, *5* (4), 655–659.

17. Mangolini, L. Synthesis, Properties, and Applications of Silicon Nanocrystals. J. Vac. Sci. Technol. B **2013**, 31, 0801

CHAPTER 4. PHOTOPHYSICAL PROPERTIES FROM DGU PURIFIED SILICON NANOCRYSTALS

4.1. Introduction

The strong dependence of SiNC electronic and optical properties on the size of nanocrystals has important implications for a number of applications, such as tailoring optoelectronic and biomedical devices with specific optical, electrical, and biological requirements. The quantum confinement effects that cause the electronic bandgap to widen, which is evident as a blueshift in the photoluminescence (PL) as the nanocrystal size decreases, portend a promising future for these materials in the field of optoelectronic nanocrystals.[1] The size dependence of the photophysical nanocrystal properties are well-studied,[2,3] including significant changes in PL QY with size.[4]

A significant concern with some nanocrystals is their potential toxicity, which is one reason to consider silicon nanocrystals (SiNCs).[5] A primary concern with SiNCs is that they are produced with considerable size polydispersity, while many applications require colloidally stable nanocrystals that are size monodisperse. The non-negligible nanocrystal size distribution leads to a degree of broadening in the spectral features, as well as ensemble average effects in the PL quantum yield.[4]

Many methods have been employed to produce monodisperse SiNCs, such as the method of size-selective precipitation.[6,7] In this chapter, however, density-gradient ultracentrifugation (DGU) is used to purify and partially narrow the size distribution of 1-dodecene passivated SiNCs.[8,9] In this work, for the first time for SiNCs derived from CHS using a non-thermal plasma reactor, we report the size dependent photoluminescence quantum efficiency, radiative lifetime, and PL peak energy for various monodisperse fractions of 1-dodecene-capped SiNCs.

4.2. Results and discussion

The 1-dodecene-passivated SiNCs samples used in this study were synthesized with cyclohexasilane (Si_6H_{12}) using a non-thermal plasma reactor. Our group used the DGU technique with mixed organic solvents in polyvinylidene fluoride ultracentrifuge tubes as a way to separate the SiNCs into monodisperse fractions. A glove box was used to extract size-separated fractions under a nitrogen atmosphere. The size-separated fractions were concentrated under a nitrogen atmosphere to boost the signal for lifetime measurements. During all PL characterization measurements, the fractions were kept in sealed 2 mL vials to prevent exposure to the ambient environment.

Figure 4.1 shows a plot of the energy of peak PL emission (375 nm excitation) as a function of nanocrystal diameter (a), PL spectra from the SiNC fractions (b), and full width at half maximum (FWHM) versus PL peak for size-purified SiNC samples (c). In **Figure 4.1a**, the quantum confinement model that describes the data is $E = E_0 + A/(2R)^a$, with $E_0 = 1.12$ eV, $A = 3.24$, and $a = 1.5$.

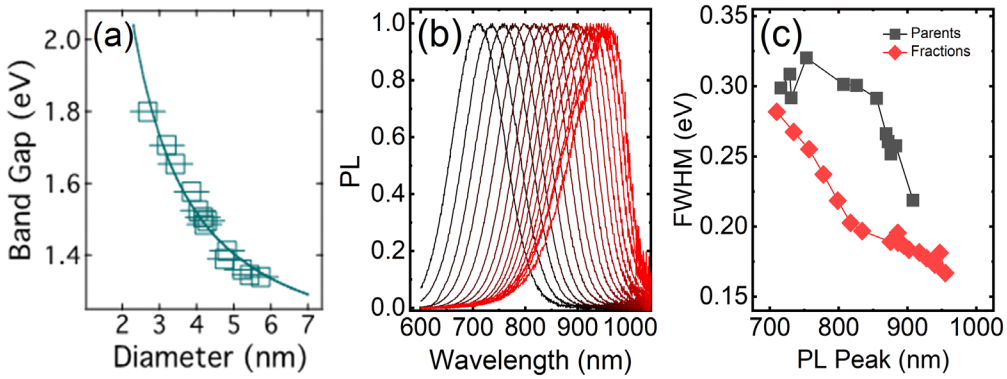

Figure 4.1: (a) PL peak energy vs. SiNC size. The SiNC size was determined from TEM measurements. (b) PL intensity of select fractions excited at 375 nm. (c) FWHM versus PL peak measured for selected fractions.

Figure 4.1b shows the typical spectra of samples that were used for the TEM study. Increasing fraction number (or PL peak wavelength) indicates a greater depth in the

polyvinylidene fluoride ultracentrifuge tube and a larger SiNC size. **Figure 4.1c** shows the values of FWHM for the selected fractions in comparison to the parent suspensions. The reduction in FWHM is dictated by the details of the separation and the initial size distribution.[10,11]

Figure 4.2 a-c shows the QY versus fraction number for three different size-separation DGU runs on three different parent suspensions. The general behavior is that the QY value starts to increase until it achieves the maxima of the curve, after which it starts to decrease. The difference can be attributed to both differences in nanocrystal size, which increases from left to right, and variations in the duration of DGU: 18 and 12 hours for the parents with 730 nm and 908 nm PL peaks, respectively, and 7 hours for 866 nm. The drop in QY with decreasing fraction number at low fraction numbers is indicative of the influence of surface effects, which have been associated with increased non-radiative recombination.[12]

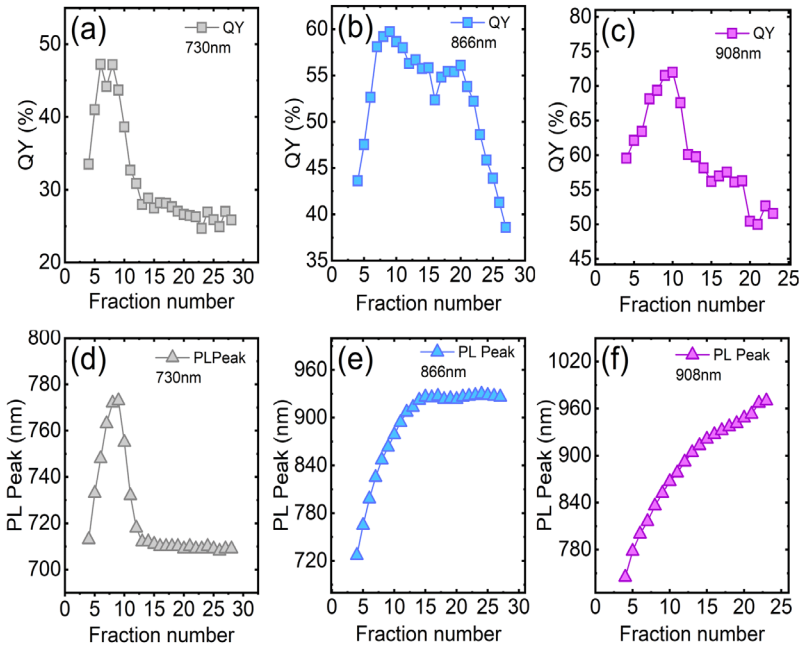

Figure 4.2: QY versus function number (equivalent to depth in the centrifuge tube measured in units of 2 mm) for DGU fractions obtained from parent SiNC suspension with PL peak of 730 nm (a), 866 nm (b), and 908 nm (c). PL peak versus function number for DGU fractions obtained from parent SiNC suspension with PL peak of 730 nm (d), 866 nm (e), and 908 nm (f).

Figure 4.2 d-f presents the behavior of the PL peak versus fraction number for the same three DGU runs. The noticeable monotonic increase in the PL peak with increasing DGU fraction number (increasing size of SiNCs) appears to be consistent with quantum confinement of the SiNCs, and provides strong evidence that DGU separation is achieved based on size. The best representation of this is in **Figure 5.2f**. In **Figure 4.2d**, the PL peak curve exhibits a different trend, where the curve increases to achieve the highest PL peak value but then exhibits a blue-shifted behavior. The initial redshift originates from the size separation of the nanocrystals,[13] while, the monotonic decrease in the PL peak could indicate incomplete surface passivation and/or insufficient DGU time. Although oxidation can lead to similar behavior,[14-17] the samples used here were shielded from ambient conditions.

Figure 4.3 shows the quantum yield and lifetime data for the selected fractions from the mentioned three spins. We chose the first five fractions from spin one (730 nm PL peak) and the first seven fractions from spin two and seven fractions from spin three (866 nm PL peak and 980 nm PL peak, respectively) for the lifetime study. **Figure 4.3a** shows the absolute QYs of the DGU fractions from the three spins as a function of the PL peak, where the QY was measured with an integrating sphere and an excitation source of 375 nm.

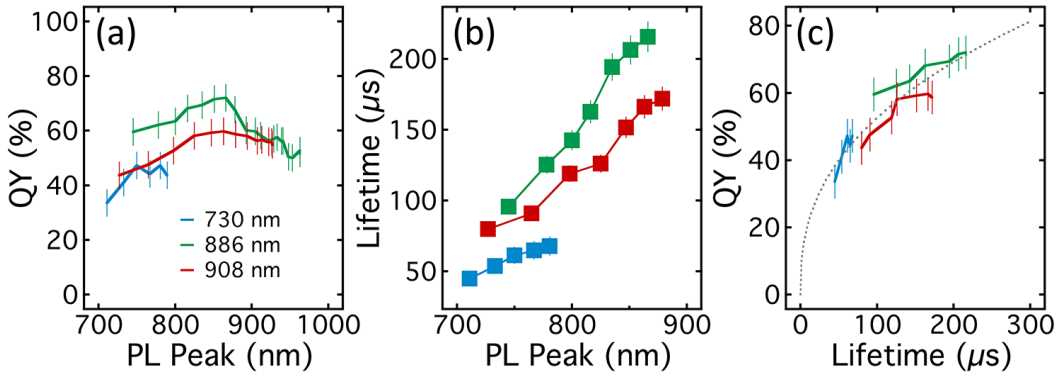

Figure 4.3: (a) QY versus PL peak emission wavelength of select SiNC DGU spins. (b) Slow relaxation time versus PL peak emission wavelength of select SiNC DGU spins.

The general behavior of the QY in the three groups of fractions agrees with the idea of competition between the radiative recombination rate and an increase in the number of surface defects for smaller nanocrystals.[18,19] The disparity of the highest QY value among the three spins could be related to the average size of the parents, with a maximum near a PL peak of 860 nm, which roughly corresponds to the Bohr exciton radius of silicon.[19,20]

4.3. Conclusion

In summary, by separating three SiNC samples into size-resolved fractions using DGU, we can gain insight into the size-dependence of the bandgap. The behavior of the QY and PL peak data for the three spins fractions appears to be consistent with quantum confinement of the SiNCs. The highest QY value, 70 %, is associated with the PL peak of around 860 nm.

4.4. Bibliography

1. Talapin, D. V.; Lee, J.-S.; Kovalenko, M. V.; Shevchenko, E. V. Prospects of Colloidal Nanocrystals for Electronic and Optoelectronic Applications. *Chem. Rev.* **2010**, *110* (1), 389–458.

2. Chaudhri, M.; Vohra, A.; Chakarvarti, S. K. Thermal Annealing Effects on Cu–Se Resonant Tunneling Diodes Fabricated by Electrodeposition-Assisted Template Synthesis Technique. *Materials Science and Engineering: B* **2008**, *149* (1), 7–11.

3. Li, M.; Li, J. C. Size Effects on the Band-Gap of Semiconductor Compounds. *Materials Letters* **2006**, *60* (20), 2526–2529.

4. Cheng, K.-Y.; Anthony, R.; Kortshagen, U. R.; Holmes, R. J. High-Efficiency Silicon Nanocrystal Light-Emitting Devices. *Nano Lett.* **2011**, *11* (5), 1952–1956.

5. Derfus, A. M.; Chan, W. C. W.; Bhatia, S. N. Probing the Cytotoxicity of Semiconductor Quantum Dots. *Nano Lett.* **2004**, *4* (1), 11–18.

6. Li, X.; He, Y.; Swihart, M. T. Surface Functionalization of Silicon Nanoparticles Produced by Laser-Driven Pyrolysis of Silane Followed by HF−HNO $_3$ Etching. *Langmuir* **2004**, *20* (11), 4720–4727.

7. Mastronardi, M. L.; Maier-Flaig, F.; Faulkner, D.; Henderson, E. J.; Kübel, C.; Lemmer, U.; Ozin, G. A. Size-Dependent Absolute Quantum Yields for Size-Separated Colloidally-Stable Silicon Nanocrystals. *Nano Lett.* **2012**, *12* (1), 337–342.

8. Van Sickle, A. R.; Miller, J. B.; Moore, C.; Anthony, R. J.; Kortshagen, U. R.; Hobbie, E. K. Temperature Dependent Photoluminescence of Size-Purified Silicon Nanocrystals. *ACS Appl. Mater. Interfaces* **2013**, *5* (10), 4233–4238.

9. Wheeler, L. M.; Anderson, N. C.; Palomaki, P. K. B.; Blackburn, J. L.; Johnson, J. C.; Neale, N. R. Silyl Radical Abstraction in the Functionalization of Plasma-Synthesized Silicon Nanocrystals. *Chem. Mater.* **2015**, *27* (19), 6869–6878.

10. Miller, J. B.; Van Sickle, A. R.; Anthony, R. J.; Kroll, D. M.; Kortshagen, U. R.; Hobbie, E. K. Ensemble Brightening and Enhanced Quantum Yield in Size-Purified Silicon Nanocrystals. *ACS Nano* **2012**, *6* (8), 7389–7396.

11. M. J. A. de Dood, Ph.D. thesis, Utrecht University, **2002**.

12. Li, Q.; Luo, T.-Y.; Zhou, M.; Abroshan, H.; Huang, J.; Kim, H. J.; Rosi, N. L.; Shao, S.; Jin, R. Silicon Nanoparticles with Surface Nitrogen: 90% Quantum Yield with Narrow Luminescence Bandwidth and the Ligand Structure Based Energy Law. ACS Nano **2016**, 10, 8385−8393.

13. Dohnalová, K.; Ondič, L.; Kůsová, K.; Pelant, I.; Rehspringer, J. L.; Mafouana, R.-R. White-Emitting Oxidized Silicon Nanocrystals: Discontinuity in Spectral Development with Reducing Size. *Journal of Applied Physics* **2010**, *107* (5), 053102.

14. Kůsová, K.; Cibulka, O.; Dohnalová, K.; Pelant, I.; Valenta, J.; Fučíková, A.; Žídek, K.; Lang, J.; Englich, J.; Matějka, P.; et al. Brightly Luminescent Organically Capped Silicon Nanocrystals Fabricated at Room Temperature and Atmospheric Pressure. *ACS Nano* **2010**, *4* (8), 4495–4504.

15. Mastronardi, M. L.; Chen, K. K.; Liao, K.; Casillas, G.; Ozin, G. A. Size-Dependent Chemical Reactivity of Silicon Nanocrystals with Water and Oxygen. *J. Phys. Chem. C* **2015**, *119* (1), 826–834.

16. Marinins, A.; Zandi Shafagh, R.; van der Wijngaart, W.; Haraldsson, T.; Linnros, J.; Veinot, J. G. C.; Popov, S.; Sychugov, I. Light-Converting Polymer/Si Nanocrystal Composites with Stable 60–70% Quantum Efficiency and Their Glass Laminates. *ACS Appl. Mater. Interfaces* **2017**, *9* (36), 30267–30272.

17. Mastronardi, M. L.; Maier-Flaig, F.; Faulkner, D.; Henderson, E. J.; Kübel, C.; Lemmer, U.; Ozin, G. A. Size-Dependent Absolute Quantum Yields for Size-Separated Colloidally-Stable Silicon Nanocrystals. *Nano Lett.* **2012**, *12* (1), 337–342.

18. Mastronardi, M. L.; Maier-Flaig, F.; Faulkner, D.; Henderson, E. J.; Kübel, C.; Lemmer, U.; Ozin, G. A. Size-Dependent Absolute Quantum Yields for Size-Separated Colloidally-Stable Silicon Nanocrystals. *Nano Lett.* **2012**, *12* (1), 337–342.

19. Takagahara, T.; Takeda, K. Theory of the Quantum Confinement Effect on Excitons in Quantum Dots of Indirect-Gap Materials. *Phys. Rev. B* **1992**, 46, 15578-15581.

20. Lorenzo, P. and Rasit, T. Silicon Nanocrystals, Mörlenbach: Wiley-VCH Verlag, **2010**.

CHAPTER 5. RADIATIVE RELAXATION IN LUMINESCENT SILICON NANOCRYSTAL THIOL-ENE COMPOSITES

5.1. Introduction

Colloidal semiconductor nanocrystals have emerged as materials of significant interest for a variety of potential applications in displays, solar energy, and medicine,[1,2] with bright tunable photoluminescence (PL) being high on the list of desirable physical attributes. For colloidal nanocrystals in general, it has long been appreciated that the nanocrystal surface plays a critical role in shaping the nature of the photo-physical response, including PL quantum yield (QY).[3,4] Effective and appropriate surface passivation is therefore critical for achieving efficient nanocrystal emission, particularly for hydride terminated-silicon nanocrystals, which require a significant degree of strong surface passivation through covalent Si-C bonds in order to achieve bright luminescence and colloidal stability in organic solvents.[5-7] Although the most commonly used passivation approach is thermal hydrosilylation,[8] there are in fact a number of different routes to the effective surface functionalization of nanocrystalline silicon.[9-11]

In certain applications like solar windows,[2] it is often required that the nanocrystals be dispersed at low concentration in a glass or polymer matrix while retaining the bright PL characteristic of the original colloid.[12-16] In general, ternary mixtures of colloidal nanocrystals, solvent, and polymer[17] (as well as mixtures of nanocrystals, solvent, and free ligand)[18,19] can exhibit liquid-liquid phase separation upon drying, and scrutiny must therefore be applied when assessing the dispersion state of nanocrystals in the surrounding material. In strongly segregated systems, for example, nanocrystal-nanocrystal interaction effects may need to be considered when evaluating ensemble luminescence QY.[20,21] However, for dilute, non-interacting

nanocrystals with simple hydrocarbon ligands strongly bound to the surface (*e.g.,* silicon), it is reasonable to expect that polymer matrices will have a neutral impact on PL QY.

In contrast to the more familiar solution-processed direct-bandgap materials such as cadmium selenide, indium phosphide, and the much-heralded lead-halide perovskites, colloidal silicon nanocrystals (SiNCs) exhibit PL that is strongly shaped by the indirect nature of the fundamental bandgap, with large Stokes shifts, broad PL linewidths, and long PL lifetimes accompanied by a wide distribution of decay rates.[22-27] Nonetheless, properly passivated nanocrystalline silicon offers an earth-abundant and nontoxic alternative for a range of potential light-harvesting, sensing, and biomedical applications, with PL QYs of up to 60-70 % across the red to the near-infrared (NIR).[28-30] In addition to the slow microsecond radiative decay characteristic of the indirect bandgap, a number of recent studies have also explored much faster (nanosecond) PL decay modes observed at shorter wavelengths, with a variety of interpretations related to quasi-direct recombination and/or surface effects at smaller nanocrystal sizes.[30-38] Indeed, photophysical processes at the nanocrystal surface remain a subject of significant current debate,[7] while the surface also presents potentially untapped opportunities for improvements in material performance.

One such area of interest is co-passivation through the simultaneous use of multiple surface chemistries, which is utilized with great effect for perovskite[12] and III-V compound nanocrystals[39] and to improve the performance of CdSeTe solar cells.[40] In the specific case of silicon, the actual fraction of ligand-capped surface atoms is only around 40 % of the total number of available sites,[30,41,42] suggesting significant room for improvement. Along these lines, recent work by Marinins *et al.*[15] explored the photoluminescent properties of hybrid composites consisting of an off-stoichiometric thiol-ene[43] (OSTE) polymer matrix loaded with alkene-

terminated SiNCs. Thiols have long been used to passivate direct bandgap nanocrystals, such as CdSe,[44] PbS,[45] and $CuInS_2$.[46] For OSTE polymer/SiNC hybrids, UV initiated thiol-ene photopolymerization is based on the addition of a thiol group to the C=C ene bond, with excess active thiyl and carbon radicals (a species hypothetically capable of nanocrystal surface passivation) controlled through the thiol/allyl ratio. UV initiation and curing of these resins is quite fast (seconds) and the rapid OSTE cascade polymerization relies on the formation of thiyl radicals created by the extraction of hydrogen radicals from the thiol resin.[43]

Here, we explore the PL relaxation landscape of this type of photo-polymerized OSTE polymer/SiNC hybrid. We find time- and air-stable emission from dilute composites with PL peaks spanning 700-950 nm and QYs of up to 70 %, and we measure the kinetics of PL relaxation in the parameter space of nanocrystal size and temperature, focusing on changes in the partitioning of multimodal decay upon going from colloid to composite. Our results reveal striking similarities between the impacts of crosslinking and those of cooling to cryogenic temperatures, but with a limited overall impact on the efficiency of emission. In the interpretation put forth here, quasi-direct radiative recombination is enhanced by the reduced availability of phonons in the polymer matrix, but with relatively little impact on the partitioning of QY between the dominant slow channel and the surface dominated fast channel.

5.2 Results and discussion

Synthetically, there are several available options for making colloidal SiNCs, but the approach used here is the nonthermal plasma method.[28,30,39,47,48] We use liquid cyclohexasilane (CHS) to make the nanocrystals, which has recently been demonstrated as a promising precursor for the plasma synthesis of SiNCs.[30] The SiNCs were thermally passivated for at least 3 h with *1*-dodecene in mesitylene to provide surface passivation and colloidal solubility. As a starting

material, we use colloidal SiNC samples with PL peaks varying from 700 nm to 950 nm that have been shielded from ambient oxygen throughout the entire synthesis/passivation/compositing process. Although a variety of size purification routes are available,[20,30,49-52] we opt here for as-prepared colloidal SiNCs without size separation. Based on transmission-electron microscopy (TEM), typical polydispersity indices (defined as $1 + \langle \delta R^2 \rangle / \langle R \rangle^2$, where R is the SiNC radius and δR is the deviation from the mean) range from 1.01 to 1.04. Using the size-resolved PL metric described in Ref. [30], the range of PL peaks explored here roughly corresponds to nanocrystal diameters of 3-7 nm. TEM images and SiNC size histograms are presented in **Figure 5.1**. Although QY can vary with solvent,[53] all the colloidal suspensions considered here were suspended in mesitylene.

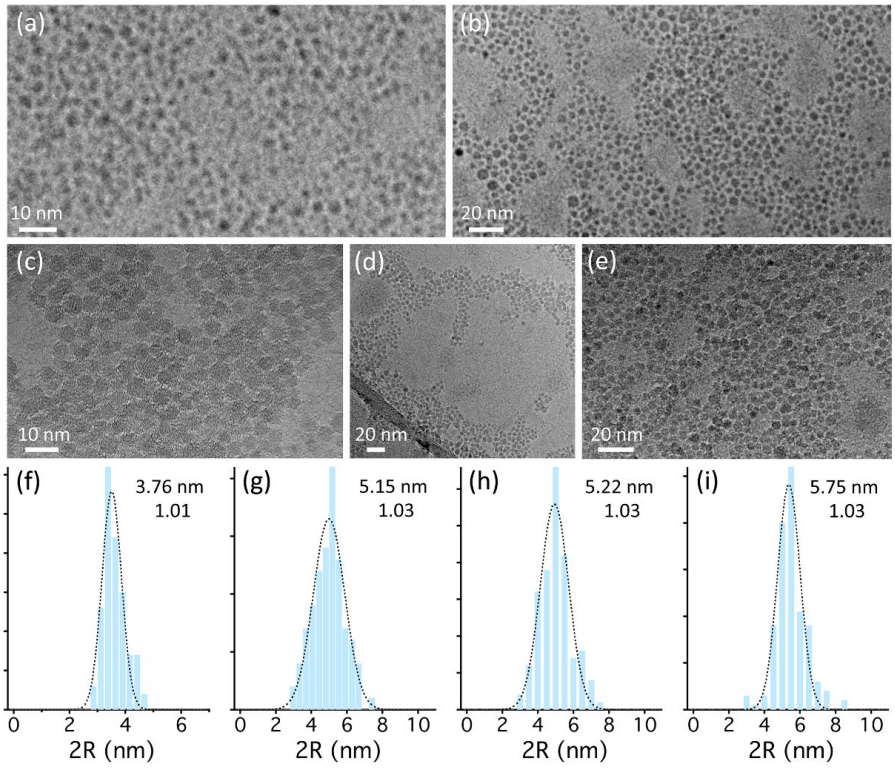

Figure 5.1: (a)-(e) Typical TEM image of SiNC colloids (PL peak near 750 nm, 875 nm, 900 nm, 900 nm, 930 nm, respectively) and size histograms based on TEM for samples with PL peaks near (f) 750 nm, (g) 875 nm, (h) 900 nm, and (i) 930 nm. Average size and polydispersity index are indicated next to each histogram.

The PL spectra of a series of colloid/composite samples are highlighted in **Figure 5.2a-b**, where the absorption band of the polymer matrix near 900 nm is evident (**Figure 5.2b**). The typical appearance of two SiNC-free reference samples (mesitylene/1-dodecene and OSTE polymer/mesitylene/1-dodecene) and an OSTE polymer/SiNC composite (all under 365 nm LED excitation) are presented in **Figure 5.2c**, while **Figure 5.2d** compares the appearance of the OSTE polymer/mesitylene/1-dodecene reference with a composite under ambient light.

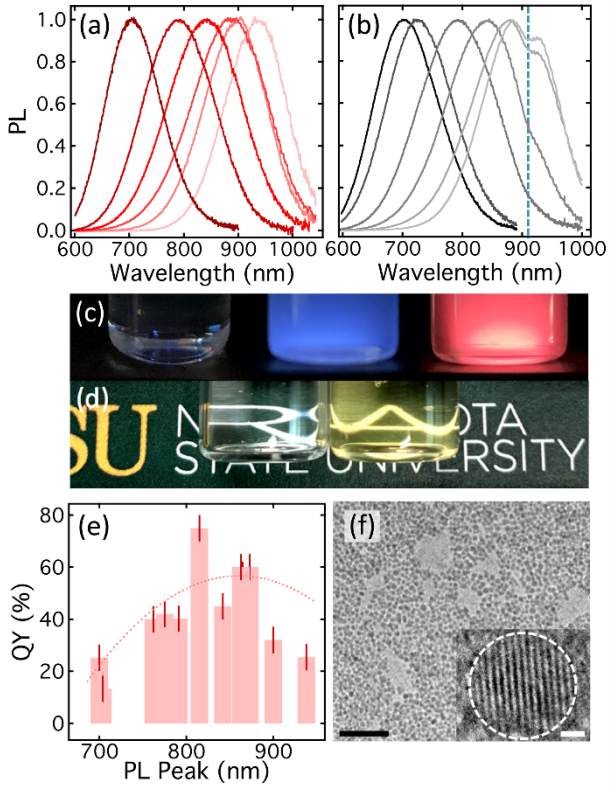

Figure 5.2: (a)-(b) PL spectra of a series of colloidal SiNC suspensions (left) and a series of composites (right). The vertical dashed line in (b) indicates an absorption band in the polymer matrix. (c) Mesitylene/1-dodecene reference (left), OSTE polymer reference (middle), and an OSTE polymer/SiNC composite (right). All three samples are being excited at 365 nm. (d) Appearance of an OSTE polymer reference (left) and an OSTE polymer/SiNC composite (right). (e) QY *vs*. peak PL wavelength for colloidal suspensions, where the red curve represents the trend reported in Ref. 30. (f) TEM image of a dried colloid (50 nm scale) and inset TEM image of an individual SiNC (1 nm scale) from a sample with a PL peak at 850 nm.

Under UV excitation, the pure resin shows scattering with respect to the solvent, indicative of underlying structural inhomogeneity and haze. The composite microstructure

consists of fine SiNC-rich domains dispersed in a cross-linked polymer matrix (**Figure 5.3**), where this type of phase-separated morphology is in general rather difficult to avoid.

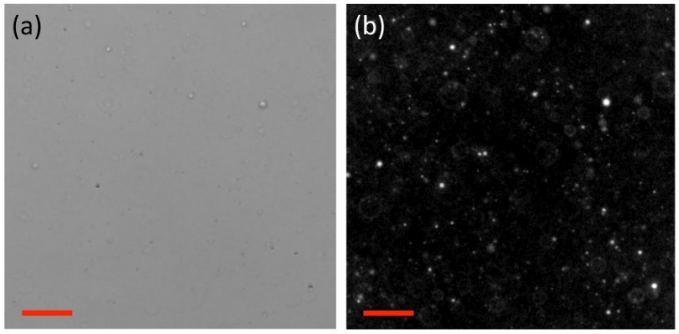

Figure 5.3: (a)-(b) Bright-field (left) and PL (right) microscopy images of a typical composite, where images were taken in transmission (left) and EPI illumination (right) on the vial in which the composite was made. Scale bar is 50 μm.

For the majority of samples, we found little difference between the QY of the colloid and that of the composite as measured in the usual manner in an integrating sphere. Some of the samples suggested a QY enhancement upon compositing, which might be interpreted through a possible co-passivation effect.[15] However, we emphasize that measuring the QY of the composites in an integrating sphere is intrinsically problematic because of strong UV absorption in the resin (**Figure 5.4**) and scattering from large-scale inhomogeneities in the polymer samples (both with and without SiNCs). This potentially clouds a quantitative interpretation of absorption changes, which in turn makes it difficult to properly quantify QY.[54]

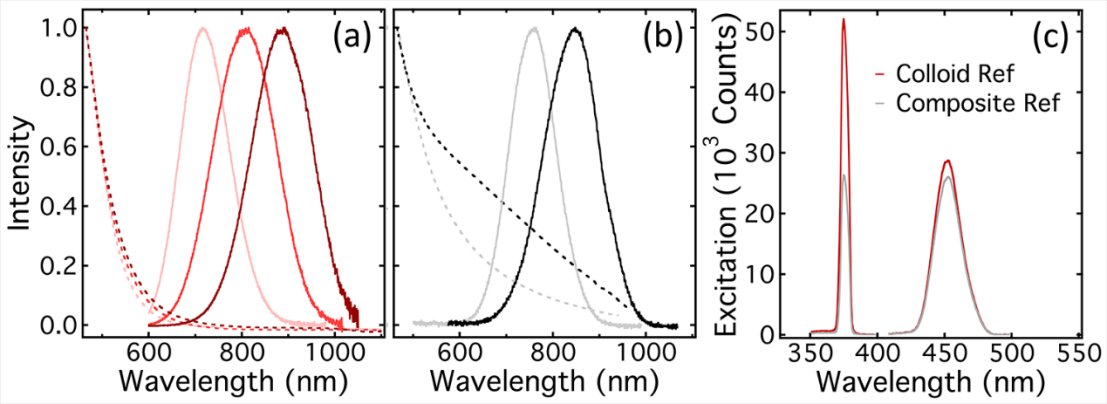

Figure 5.4: (a) Representative PL spectra (solid) and the corresponding absorption spectra (dashed) for colloidal SiNCs in mesitylene. PL spectra are normalized to 1 at the peak and absorption is normalized to 1 at 465 nm. (b) A similar plot for SiNC composites, where the pure resin has been used as the reference for absorption measurements. (c) Comparison of the extinction between colloid and composite references (no SiNCs) for two optical inputs (375 nm laser and 450 nm LED). The composites show anomalously strong absorption, which we attribute to a combination of optical turbidity, structural inhomogeneity, and the strong optical absorption of the pure resin at short wavelengths.

Care must therefore be taken when interpreting the measured QY of the composites, and we return to this question later in the discussion. With this in mind, composite QY measured in an integrating sphere, where reported, used a 473 nm laser, whereas the colloid QY was unchanged using either 375 nm or 473 nm excitation.

Figure 5.5 shows PL relaxation curves for the samples depicted in **Figure 5.2a-b**. Measurement details can be found in Chapter 2. We normalize the response to unity at $t = 0$ (as opposed to normalizing to SiNC concentration)[30] to remove variations in overall intensity. As in numerous previous studies,[30-38] we observe both a 'fast' (ns) decay and a slow (μs) decay, where our interpretation is that the latter is associated with phonon-assisted recombination across the fundamental (indirect) bandgap while the former reflects quasi-direct (zero-phonon) recombination arising from the influence of interfacial effects at the nanoscale.[30] The decay is fit to the expression

$$I(t) = A_f \exp\left[-\left(\frac{t}{\tau_f}\right)^{\alpha_f}\right] + A_s \exp\left[-\left(\frac{t}{\tau_s}\right)^{\alpha_s}\right] \quad (5.1)$$

where A is relaxation amplitude, τ is lifetime, α is stretching exponent, and the subscripts f and s denoted "fast" and "slow", respectively. Representative decay curves are shown in **Figure 5.5a-b**. Stretched-exponential decays are commonly observed for SiNCs and indicate a broad range of relaxation rates, even in size-purified nanocrystals.[30,53] For the normalization used here, the fast and slow amplitude are constrained to sum to 1. Additional decays with accompanying fits and a table of all physical and fitting parameters can be found in **Figure 5.5**, **Tables 5.1** & **5.2**.

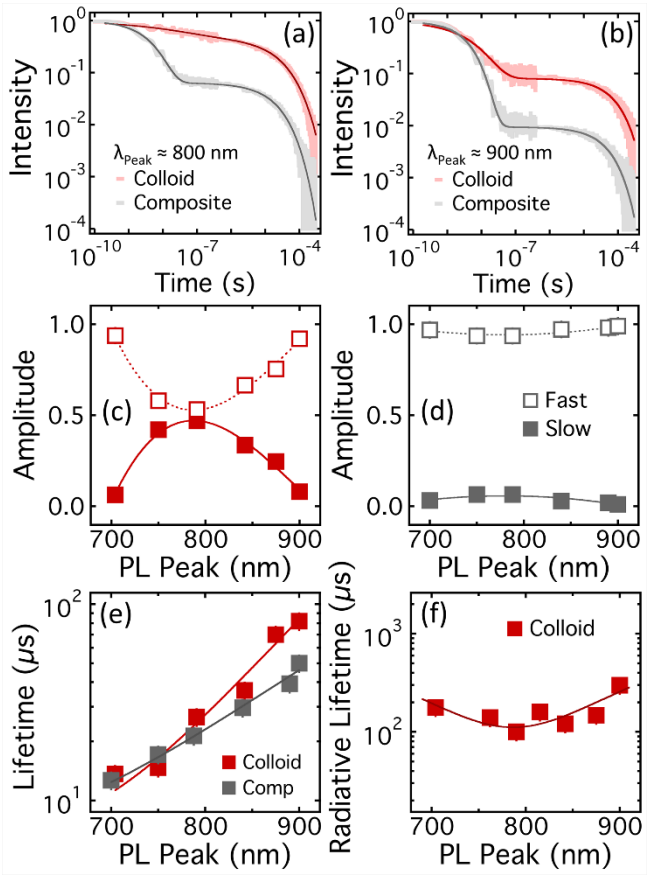

Figure 5.5: (a)-(b) Representative PL relaxation curves for colloidal and composite samples (excitation at 375 nm). (c) Fast (open) and slow (closed) amplitude as a function of PL peak for colloidal samples (red) and (d) composites (gray). (e) Slow lifetime of the colloid and composite samples. (f) Radiative lifetime deduced from the measured QY as a function of PL peak wavelength for the colloidal samples.

The amplitudes, A_f and A_s, show strikingly different behavior in the colloid as compared to the composite (**Figure 5.5c-d**). For the colloidal samples (**Figure 5.5c**), the slow mode

becomes most pronounced near a PL peak of 800 nm, where the fast mode is reduced in amplitude. Using the size metric recently obtained for pristine size-purified SiNCs synthesized in the same reactor,[30] this roughly corresponds to a mean SiNC diameter of 4 nm. Recent work on size-purified SiNC fractions extracted from a parent synthesized near the QY maximum (800-850 nm) revealed an increase in the fast mode intensity with increasing size that was attributed to defective/aggregated SiNCs.[30] Here, colloidal SiNCs were synthesized at conditions specifically targeting larger nanocrystal size, and the PL originates predominantly from desirable SiNCs as opposed to defective particles or aggregates (as evidenced by the symmetric PL line shape in **Figure 5.2a-b**).[30] With increasing SiNC size, the fast channel reemerges after passing through a diameter roughly corresponding to the Bohr exciton radius (4-5 nm), where the QY again decreases (**Figure 5.5c-e**). Above the confinement length scale, the exciton is free to diffuse, increasing the likelihood that it will decay nonradiatively at a defect or surface site.

In contrast to the colloidal samples, the slow mode is significantly suppressed in the composites for all SiNC sizes studied (**Figure 5.5d**), while the PL lifetime τ_s increases with increasing nanocrystal size in both colloid and composite, although less rapidly in the latter (**Figure 5.5e**). To explain the trends in Figure 9.4, we consider the physical origin of each term in **Eq. 5.1**.

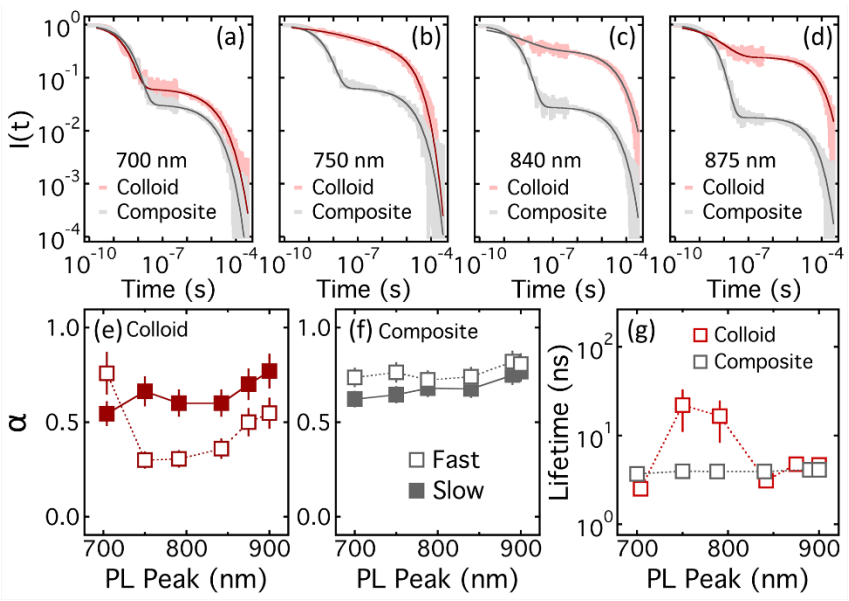

Figure 5.6: (a)-(d) Additional PL relaxation curves with the corresponding fits. The PL peak of each sample is indicated. (e) Fast (open) and slow (closed) stretching exponents as a function of PL peak for the colloidal samples, and (f) a similar plot for the composite samples. (g) Fast lifetime *vs*. PL peak for colloids and composites. For the colloid, the increase in τ_f and the increase in stretching (small α_f) near 800 nm correlate with the maximum in A_s of the spectrally integrated intensity.

Table 5.1: Characteristics and fitting parameters for the PL relaxation of the colloidal samples presented in **Figure 5.5** of the main text, where QY is reported in %. Diameter is based on TEM with polydispersity index indicated.

λ_{em} (nm)	QY (± 5%)	A_S	A_f	τ_s (µs)	τ_f (ns)	α_s	α_f	τ_{SR} (µs)	2R (mm)
704	13.30	0.062 ±0.003	0.938 ±0.003	13.65 ±1.4	2.50 ±0.2	0.54 ±0.02	0.76 ±0.11	180 ±35	-
750	-	0.042 ±0.02	0.580 ±0.02	14.70 ±1.5	22.0 ±10	0.66 ±0.02	0.3 ±0.05	-	3.76 (1.01)
790	40.2	0.047 ±0.02	0.530 ±0.02	26.6 ±2.7	16.6 ±8	0.6 ±0.02	0.31 ±0.05	100 ±20	-
842	45.00	0.034 ±0.02	0.660 ±0.02	36.30 ±3.6	3.10 ±0.3	0.6 ±0.02	0.36 ±0.05	120 ±24	-
875	60.10	0.025 ±0.01	0.750 ±0.01	70.0 ±7.0	4.80 ±0.5	0.7 ±0.02	0.5 ±0.08	150 ±30	5.15 (1.03)
900	32.00	0.08 ±0.004	0.920 ±0.004	82.0 ±8.2	4.70 ±0.5	0.77 ±0.02	0.55 ±0.08	300 ±60	5.22 (1.03)

Table 5.2: Characteristics and fitting parameters for the PL relaxation of the composite samples presented in **Figure 5.5** of the main text, where QY is reported in %. *Indicates QY as measured in an integrating sphere.

λ_{em} (nm)	QY ($\pm$ 5%)	A_S	A_f	τ_s (µs)	τ_f (ns)	α_s	α_f	τ_{SR} (µs)	2R (mm)
704	17.70	0.031 $\pm$0.002	0.969 $\pm$0.002	12.70 $\pm$1.3	3.70 $\pm$0.4	0.62 $\pm$0.02	0.74 $\pm$0.11	11 $\pm$3	-
750	-	0.064 $\pm$0.003	0.936 $\pm$0.003	17.1 $\pm$1.7	3.90 $\pm$0.4	0.66 $\pm$0.02	0.76 $\pm$0.05	-	3.76 (1.01)
788	51.2	0.064 $\pm$0.003	0.936 $\pm$0.003	21.3 $\pm$2.1	3.90 $\pm$0.4	0.6 $\pm$0.02	0.72 $\pm$0.05	32 $\pm$8	-
840	47.90	0.028 $\pm$0.001	0.972 $\pm$0.001	29.70 $\pm$3.0	3.90 $\pm$0.4	0.6 $\pm$0.02	0.74 $\pm$0.05	37 $\pm$10	-
890	61.7	0.018 $\pm$0.001	0.982 $\pm$0.001	39.30 $\pm$4.0	4.10 $\pm$0.4	0.7 $\pm$0.02	0.82 $\pm$0.06	34 $\pm$9	5.15 (1.03)
900	51.4	0.009 $\pm$0.001	0.991 $\pm$0.001	50.0 $\pm$5.0	4.10 $\pm$0.4	0.77 $\pm$0.02	0.81 $\pm$0.06	20 $\pm$5	5.22 (1.03)

The raw intensity (prior to $A_s + A_f = 1$ normalization) contains at least two stretched-exponential decays, indicative of a broad distribution of relaxation rates in each channel, fast (*f*) and slow (*s*).[53,55] The amplitude of each decay is the product of the associated fraction of emitters and radiative rate constant, $k_{i_\mathrm{R}} = 1/\tau_{i_\mathrm{R}}$ (*i* = *s* or *f*), which follows from fact that the PL intensity is the term proportional to k_{i_R} in the time-derivative of the fraction of excited emitters.[55] The QY can then be obtained as the time integral of the PL intensity. Despite the fact that the fast mode dominates the dynamic intensity, particularly for the composites (**Figure 9.4d and Figure 5.7a**), the slow mode dominates the QY for all samples (**Figure 5.7b**).

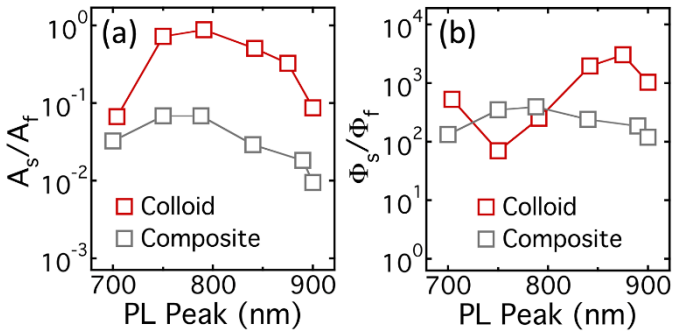

Figure 5.7: (a) The ratio of slow to fast relaxation amplitude, A_s/A_f, as a function of PL peak, and (b) the corresponding implied ratio ($\Phi_s/\Phi_f = \left(\frac{A_s}{A_f}\right)\left(\frac{\tau_s}{\tau_f}\right)\left(\frac{\alpha_f}{\alpha_s}\right)\frac{\Gamma(\alpha_s^{-1})}{\Gamma(\alpha_f^{-1})}$) of the slow to fast contributions to the QY for colloidal (red) and composite (gray) samples.

This allows us to express the radiative lifetime of the slow mode, τ_{s_R}, in terms of the QY (Φ), τ_s, and α_s through $\Phi \approx (\tau_s/\tau_{s_R})\,\Gamma(\alpha_s^{-1})/\alpha_s$. Because we measure the QY, τ_s, and α_s for the colloid, we can thus extract radiative lifetime, assumed here to be independent of state, which is plotted *versus* PL peak in **Figure 5.5f**. In this view, the drop in slow lifetime in **Figure 5.5e** is indicative of a decrease in QY on going from colloid to composite.

Figure 5.8 expands on the preceding analysis with additional samples and measurements, including two examples that showed little change in QY as measured in an integrating sphere (**Figure 5.8a-b**). The PL decay curves of these two samples show the same trends as the data in **Figure 9.4c-d**, which is specific to compositing (gray) and not simply drying (orange) the colloid (red). The curves are the bimodal relaxation described by **Eq. 5.1**, with the fitting parameters and QY summarized in **Table 5.3**.

Table 5.3: Characteristics and fitting parameters for the PL relaxation of the colloidal samples presented in **Figure 5.8** of the main text, where QY is reported in %. Dried colloidal samples are exposed to air and hence will have a lower QY, which is apparent here as a shorter lifetime. *Indicates QY as measured in an integrating sphere.

Sample (Fig. 5.5a)	**λ_{em} (nm)**	**A_S**	**A_f**	**τ_s (µs)**	**τ_f (ns)**	**α_s**	**α_f**	**QY (%)**
Colloid	762	0.39 ±0.02	0.61 ±0.02	33.76 ±1.6	14.00 ±5.0	0.56 ±0.02	0.31 ±0.11	0.40 ±5.0
Dried Colloid	-	0.33 ±0.02	0.67 ±0.02	8.2 ±1.0	2.5 ±0.5	0.40 ±0.02	0.61 ±0.05	-
Composite	767	0.08 ±0.02	0.92 ±0.02	32.5 ±1.6	4.5 ±0.5	0.55 ±0.02	0.78 ±0.05	33* 48±0.02

Sample (Fig. 5.5b)	**λ_{em} (nm)**	**A_S**	**A_f**	**τ_s (µs)**	**τ_f (ns)**	**α_s**	**α_f**	**QY (%)**
Colloid	815	0.47 ±0.02	0.53 ±0.02	97.7 ±1.6	3.5 ±1.0	0.71 ±0.02	0.38 ±0.11	66 ±5.0
Dried Colloid	-	0.44 ±0.002	0.56 ±0.02	47.4 ±2.0	2.15 ±0.5	0.61 ±0.02	0.35 ±0.11	-
Composite	820	0.10 ±0.02	0.90 ±0.02	69.2 ±2.5	4.5 ±0.5	0.68 ±0.02	0.72 ±0.05	68* 75±10.0

Note that the slow lifetime of these two composites is larger than those in **Figure 5.5**. As an additional – and we suggest more robust – method of determining composite QY, we use the expression $\Phi = \left(\tau_s/\tau_{s_R}\right)\Gamma(\alpha_s^{-1})/\alpha_s$, where τ_s and α_s are measured for the composite and the radiative lifetime τ_{s_R} is interpolated from **Figure 5.5f**. The derivation of this expression is given in Chapter 6. The QY of the composites determined from PL lifetime in this manner is compared with the QY of the colloidal samples (measured in an integrating sphere) in **Figure 5.8e**. Overall, PL efficiency remains the same or is slightly reduced in the composites. This is also evident in plots of the composite QY determined from lifetime plotted against the QY of the colloid (**Figure 5.8f, left**) and plotted against the QY of the composite measured in the integrating sphere (**Figure 5.8f, right**).

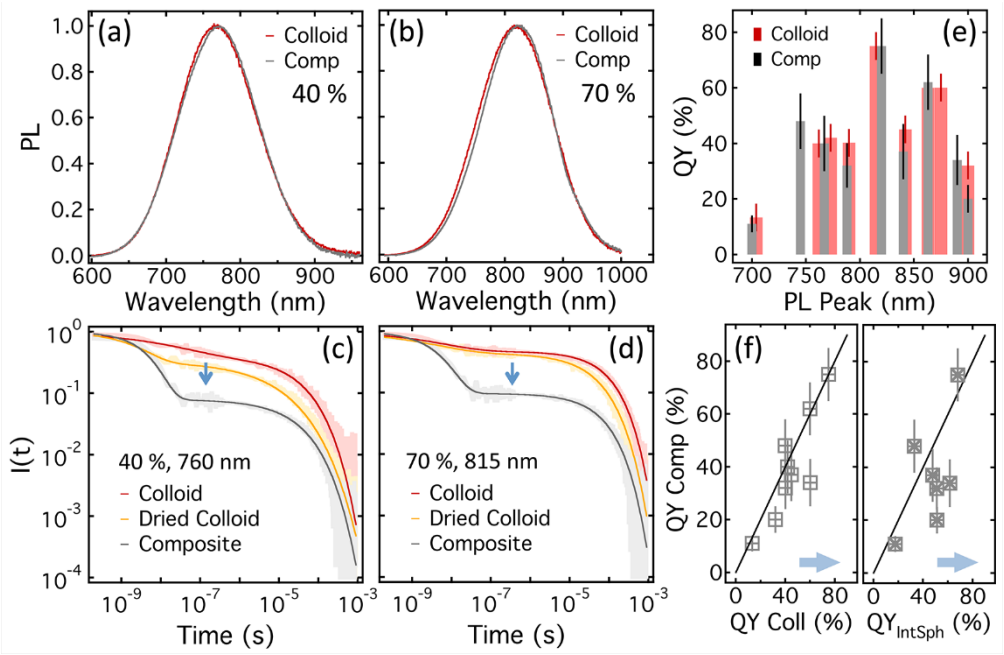

Figure 5.8: (a) PL spectra before (colloid) and after compositing (comp) for a sample with a QY of 35 %. (b) PL spectra before and after compositing for a sample with a QY of 70 %. (c)-(d) PL relaxation for colloid, dried colloid, and composite for the same two samples (375 nm excitation). The arrows indicate the direction of processing. (e) QY of colloidal (red) and composite (gray) samples, where the former is measured in an integrating sphere and the latter is determined from Pl lifetime as described in the text. (f) QY of the composites determined from PL lifetime plotted against QY of the colloid measured in an integrating sphere (left) and plotted against the QY of the composite measured in an integrating sphere (right). The arrows indicate the direction that the majority of measurements deviate from the diagonal line of equal QY.

We note that the latter suggests that the composite QY is systematically over-estimated in the integrating sphere, which we attribute to the short wavelength absorption uncertainties cited above. Although these results differ from the findings of Marinins *et al,*[15] we note that there are significant differences between the SiNCs employed here and those used in Ref. [15], including synthesis scheme. Most notably, the SiNCs used here were not "washed" with antisolvent to remove excess ligand, which leads to reduced QY with respect to the as-passivated parent. Rather, the scheme used here targets pristine as-passivated nanocrystals, with unbound ligand and any residual mesitylene incorporated into the matrix. In this scenario, our results suggest that there is no co-passivation effect.

For a final piece of insight into radiative relaxation, we turn to cryogenic PL measurements. It is well known that cooling SiNCs from ambient to low temperature (*T*) leads to an increase in QY and a subsequent increase in PL intensity and lifetime,[16,18,56-58] which is commonly ascribed to a reduction in the non-radiative rate constant on cooling (or in this case rate constants: $k_{i_{\mathrm{NR}}} = \tau_i^{-1} - \tau_{i_{\mathrm{R}}}{}^{-1}$ with *i* = *s* or *f*). Physically, the influence of non-radiative effects is suppressed at lower *T*. In concert with this change in QY, recent work also demonstrates that the partitioning of fast and slow PL also changes on cooling, with the quasi-direct channel becoming more prominent at lower *T*, despite making no meaningful contribution to the QY.[32] We note that very similar changes in partitioning are observed here on going from colloid to composite.

The cryogenic SiNC PL response can be viewed as falling into two regimes: a near-cryogenic regime at modest cooling (characterized by a rapid drop in the impact of nonradiative effects) and a far-cryogenic regime at deep cooling (close to 0 K, characterized by a relative lack of nonradiative effects but subtle changes in radiative rate).[56] The crossover temperature between these two regimes roughly coincides with 100 K,[56] and in a liquid-nitrogen setup we can thus expect to probe the near-cryogenic regime and the onset of a crossover to true cryogenic conditions. Samples utilized for cryogenic measurements in this study were primarily UV-cured composites (prepared both in-vial or on a glass coverslip), although measurements were also performed on dried colloids.

The *T* dependence of the SiNC bandgap has been studied in detail, and although a closed-form expression analogous to the Varshni equation does not exist for nanocrystalline silicon, bandgap widening is commonly observed at low temperatures[16,56-58] and the SiNCs studied here show similar behavior (**Figure 5.a**).

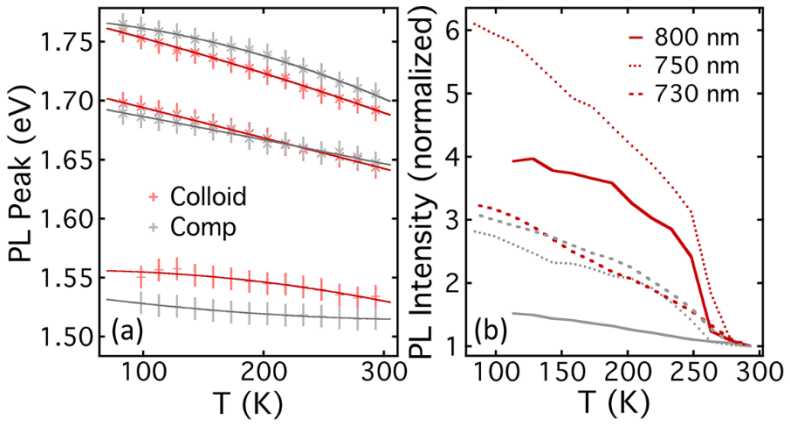

Figure 5.9: (a) Temperature dependent bandgap of three colloid/composite pairs with 2nd order polynomial fits. (b) Temperature dependent PL intensity for the data in panel (a) normalized to unity at 25 °C. Colloidal data are red and composite data are gray.

Although the PL intensity increases with decreasing *T*,[16,56] this trend can be complicated in dried colloids, where environmental factors (*e.g.*, oxygen exposure) and *T* dependent microstructure can alter the PL response in nontrivial ways.[18] Here, a comparison of the PL increase on cooling for a variety of dried colloids and the corresponding composites suggests a sample-dependent response, but with a stronger increase on cooling for dried colloids (**Figure 5.9b**), which is difficult to interpret due to the effects of ambient oxygen. In contrast, because the composites are photo-stable under atmospheric conditions, they represent a unique system for studying the cryogenic PL response.

An example of this is summarized for a composite sample in **Figure 5.10** (PL peak of 750 nm with a colloidal QY of 42 %), where both PL intensity and slow lifetime show an increase on cooling (**Figure 5.10a-b**). Interestingly, the slow relaxation becomes less "stretched" at lower *T* (**Figure 5.10c**), which is similar to what has been reported previously for dried colloids[16,32] and elastomer/SiNC composites.[16] Likewise, the fast amplitude, despite being significantly enhanced already in the composite, becomes even more prominent on cooling (**Figure 5.10c**), a trend that was previously reported for dried SiNC colloids.[32] The full

relaxation data set, along with a table of fitting parameters, can be found in **Table 5.5, Figure 5.11**.

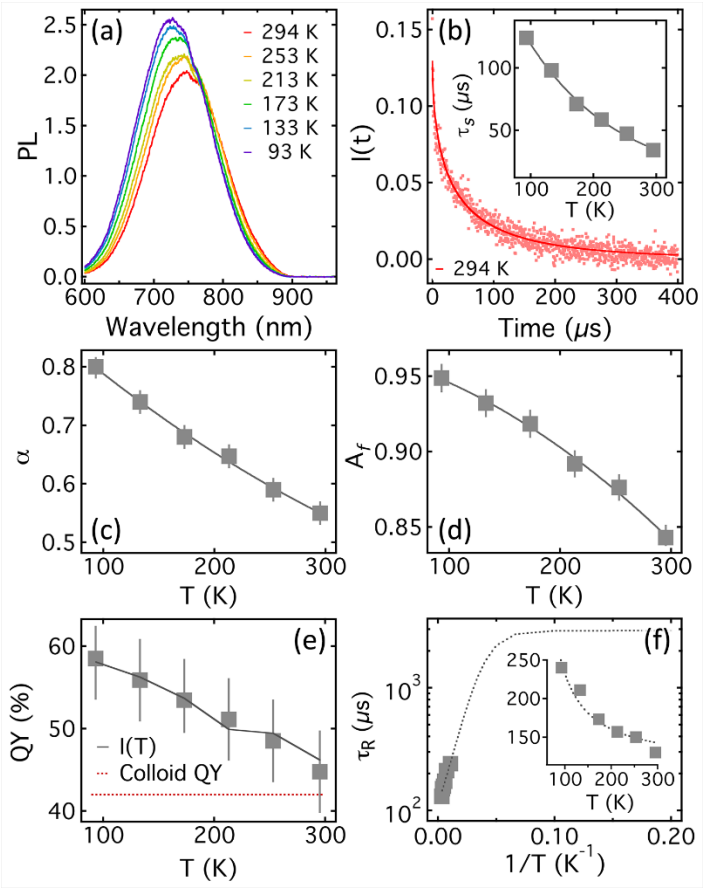

Figure 5.10: (a) Temperature dependent PL spectra of a composite. (b) Slow PL decay at ambient temperature, with slow lifetime *vs*. temperature in the inset. Time dependent decay curves for each T can be found in Fig. S7 and the fitting results are summarized in Table S4. (c) Slow stretching exponent and (d) fast amplitude *vs*. T. (e) QY deduced from $\tau_s(T)$, $\alpha_s(T)$, and $\tau_{s_R}(T)$ as detailed in the text. The horizontal dashed line is the QY of the parent colloid and the black line is the measured steady-state PL intensity (scaled onto QY). (f) T dependence of τ_{s_R} for the data in panel (e). The dashed curve is the theoretical expression derived in the text.

Table 5.4: Fitting parameters for fast and slow PL relaxation at each temperature detailed in **Figure 5.11**.

λ_{em} (nm)	QY (± 5%)	As	Af	τ_s (µs)	τ_f (ns)	α_s	α_f	τ_{SR} (µs)	2R (mm)
704	17.70	0.031 ±0.002	0.969 ±0.002	12.70 ±1.3	3.70 ±0.4	0.62 ±0.02	0.74 ±0.11	11 ±3	-
750	-	0.064 ±0.003	0.936 ±0.003	17.1 ±1.7	3.90 ±0.4	0.66 ±0.02	0.76 ±0.05	-	3.76 (1.01)
788	51.2	0.064 ±0.003	0.936 ±0.003	21.3 ±2.1	3.90 ±0.4	0.6 ±0.02	0.72 ±0.05	32 ±8	-
840	47.90	0.028 ±0.001	0.972 ±0.001	29.70 ±3.0	3.90 ±0.4	0.6 ±0.02	0.74 ±0.05	37 ±10	-
890	61.7	0.018 ±0.001	0.982 ±0.001	39.30 ±4.0	4.10 ±0.4	0.7 ±0.02	0.82 ±0.06	34 ±9	5.15 (1.03)
900	51.4	0.009 ±0.001	0.991 ±0.001	50.0 ±5.0	4.10 ±0.4	0.77 ±0.02	0.81 ±0.06	20 ±5	5.22 (1.03)

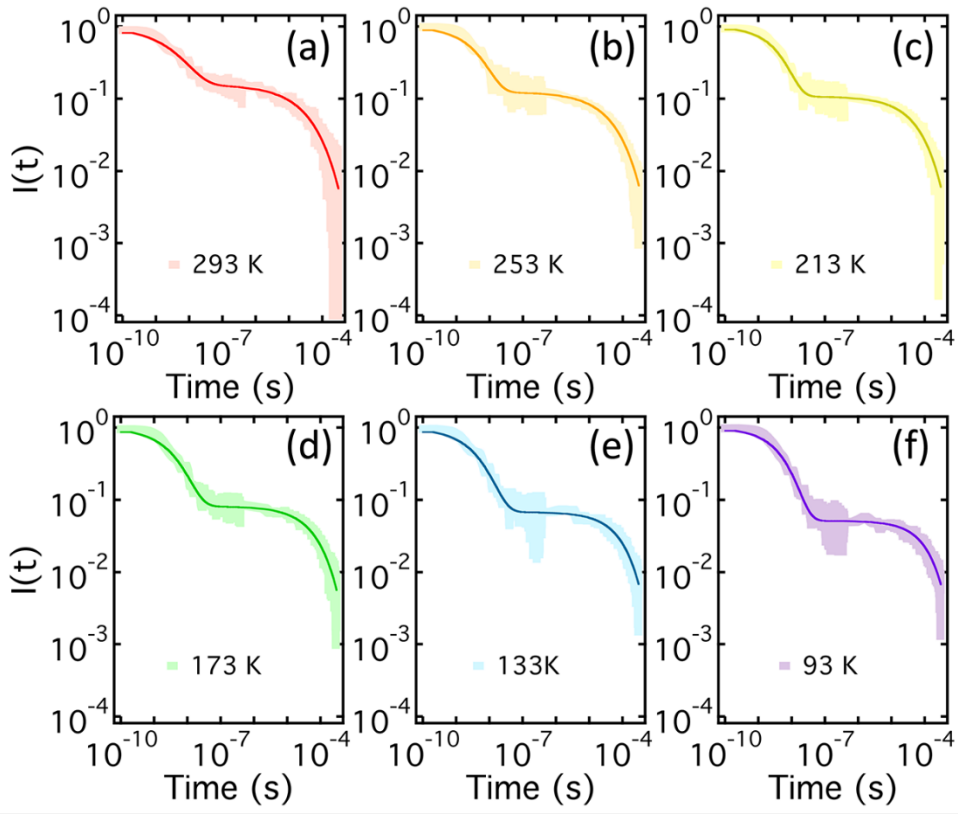

Figure 5.11: (a)-(f) Measured PL relaxation curves with fits for the temperature dependent composite detailed in the text.

We interpret these trends through the relative availability if phonons in quantum-confined nanocrystalline silicon. For SiNCs in general, the dipole matrix element – which governs light-field interactions and radiative processes – contains three contributions: zero-phonon, phonon-absorption, and phonon-emission mediated transitions,[59] where the latter two depend on a sum of occupation number over all available phonon modes. As SiNC size decreases, the combined influence of quantum confinement and surface effects increase the relative contribution of zero-phonon (quasi-direct) transitions, as recently discussed for size-dependent optical absorption[60] and PL measurements.[30] We posit that compositing the SiNCs in a crosslinked thio-lene matrix impacts the partitioning of these terms through a reduced phonon DOS, which is the origin of the enhanced fast-mode strength in the composites (**Figure 5.5c-d**). With cooling, the decrease in phonon occupation number further enhances this effect, leading to an additional increase in the amplitude of the fast mode.

Physically, the introduction of a glassy polymer matrix and cooling to cryogenic *T* both reduce the availability of phonons, although through different "handles", leading to an increased likelihood of quasi-direct (fast) recombination. It is important to note that despite these enhancements, the fast mode still makes a negligible contribution to the QY, which remains dominated by the slow mode.

We go somewhat further by reconciling the *T* dependent PL intensity (**Figure 5.10a**) with extrapolated values of QY obtained from the *T*-dependence of the slow decay (**Figure 5.10b-c**). Given that we know the relevant radiative lifetime at ambient (**Figure 5.5f**), we can exploit established models of its temperature dependence to convert $\tau_s(T)$ to QY. Specifically, the energy levels of strongly localized excitons in silicon are split by an amount Δ because of electron-hole exchange interactions, which impacts the *T* dependence of the crossover in PL to

far-cryogenic conditions. The lower level is a three-fold degenerate triplet state with lifetime τ_{T}, while the upper singlet level has lifetime τ_{S}, and thermal equilibrium between these two levels gives the radiative lifetime:[62]

$$\tau_{\mathrm{R}}(T) = \tau_{\mathrm{T}} \frac{\left(3+e^{-\beta\Delta}\right)}{\left(3+Re^{-\beta\Delta}\right)} \tag{5.2}$$

where $R = \tau_{\mathrm{T}}/\tau_{\mathrm{S}}$ and $\beta = 1/k_B T$. We have one data point on this curve (ambient *T*), so we use $\Phi = (\tau_s/\tau_{s_{\mathrm{R}}})\,\Gamma(\alpha_s^{-1})/\alpha_s$ to compute an effective $\tau_{\mathrm{R}}(T)$, constrained at ambient, that gives the same *T* dependence in Φ as measured for PL (**Figure 5.10e**). A nonlinear regression this $\tau_{\mathrm{R}}(T)$ to **Eq. 5.2** then gives $R = \tau_{\mathrm{T}}/\tau_{\mathrm{S}}$ = 100, Δ = 8 meV, and τ_{T} = 3 ms, which compare well to values in the literature measured under deep cryogenic conditions.[56,58] The data and corresponding fit are shown in **Figure 5.10f**.

5.3. Conclusion

We have explored details of PL relaxation in photo-polymerized off-stoichiometric polymer/nanocrystal hybrids. Specifically, thiol-ene polymer/nanocrystal composites were synthesized from a tetra-functional thiol, tri-functional allyl and a family of dilute dodecyl-passivated colloidal SiNCs with peak PL wavelength spanning the red to the near infrared. We find time- and air-stable emission from thiol-ene SiNC composites exhibiting to 70 % QY, with the compositing process having little apparent impact on emission efficiency. Multimodal PL relaxation has been mapped in the parameter space of nanocrystal size and state at near-cryogenic temperatures. Changes in the partitioning of fast and slow PL decay observed on going from colloid to composite are similar to those observed on cooling, where both effects reflect a loss of available phonon modes and an increase in the strength of quasi-direct emission. Despite these changes, the slow mode dominates the PL QY, by a factor 10^2 to 10^3 depending on sample quality, for all samples and temperatures studied.

5.4. Bibliography

1. Mazzaro, R.; Romano, F.; Ceroni, P. Long-Lived Luminescence of Silicon Nanocrystals: From Principles to Applications. *Phys. Chem. Chem. Phys*. **2017**, *19*, 26507−26526.

2. Meinardi, F.; Ehrenberg, S.; Dhamo, L.; Carulli, F.; Mauri, M.; Bruni, F.; Simonutti, R.; Kortshagen, U.; Brovelli, S. Highly Efficient Luminescent Solar Concentrators Based on Earth-Abundant Indirect-Bandgap Silicon Quantum Dots. *Nat. Photonics* **2017**, *11*, 177−185.

3. Boles, M. A.; Ling, D.; Hyeon, T.; Talapin, D. V. The Surface Science of Nanocrystals. *Nat. Mater*. **2016**, *15*, 141−153.

4. Lim, S. J.; Ma, L.; Schleife, A.; Smith, A. M.; Quantum Dot Surface Engineering: Toward Inert Fluorophores with Compact Size and Bright, Stable Emission. *Coord Chem Rev*. **2016**, *320-321*, 216–237.

5. Veinot, J. G. C. Synthesis, Surface Functionalization, and Properties of Freestanding Silicon Nanocrystals. *Chem. Commun*. **2006**, *40*, 4160–4168.

6. Yu, Y.; Hessel, C. M.; Bogart, T. D.; Panthani, M. G.; Rasch, M. R.; Korgel, B. A. Room Temperature Hydrosilylation of Silicon Nanocrystals with Bifunctional Terminal Alkenes. *Langmuir* **2013**, *29*, 1533–1540.

7. Sinelnikov, R.; Dasog, M.; Beamish, J.; Meldrum, A.; Veinot, J. G. C. Revisiting an Ongoing Debate: What Role Do Surface Groups Play in Silicon Nanocrystal Photoluminescence? *ACS Photonics* **2017**, *4*, 1920−1929.

8. Mangolini, L. Synthesis, Properties, and Applications of Silicon Nanocrystals. *J. Vac. Sci. Technol. B* **2013**, *31*, 0801.

9. Islam, M. A.; Mobarok, M. H.; Sinelnikov, R.; Purkait, T. K.; Veinot, J. G. C. Phosphorus Pentachloride Initiated Functionalization of Silicon Nanocrystals. *Langmuir* **2017**, *33*, 8766−8773.

10. Mobarok, M. H.; Purkait, T. K.; Islam, M. A.; Miskolzie, M.; Veinot, J. G. C. Instantaneous Functionalization of Chemically Etched Silicon Nanocrystal Surfaces. *Angew. Chem. Int. Ed*. **2017**, *56*, 6073−6077.

11. Wheeler, L. M.; Anderson, N. C.; Palomaki, P. K. B.; Blackburn, J. L.; Johnson, J. C.; Neale, N. R. Silyl Radical Abstraction in the Functionalization of Plasma-Synthesized Silicon Nanocrystals. *Chem. Mater.* **2015**, *27*, 6869−6878.

12. Kovalenko, M. V.; Protesescu, L.; Bodnarchuk, M. I. Properties and Potential Optoelectronic Applications of Lead Halide Perovskite Nanocrystals. *Science* **2017**, *358*, 745–750.

13. Marinins, A.; Yang, Z.; Chen, H.; Linnros, J.; Veinot, J. G. C.; Popov, S.; Sychugov, I. Photostable Polymer/Si Nanocrystal Bulk Hybrids with Tunable Photoluminescence. *ACS Photonics* **2016**, *3*, 1575−1580.

14. Sychugov, I.; Fucikova, A.; Pevere, F.; Yang, Z.; Veinot, J. G. C.; Linnros, J. Ultranarrow Luminescence Linewidth of Silicon Nanocrystals and Influence of Matrix. *ACS Photonics* **2014**, *1*, 998–1005.

15. Marinins, A.; Zandi Shafagh, R.; van der Wijngaart, W.; Haraldsson, T.; Linnros, J.; Veinot, J. G. C.; Popov, S.; Sychugov, I. Light-Converting Polymer/Si Nanocrystal Composites with Stable 60–70% Quantum Efficiency and Their Glass Laminates. *ACS Appl. Mater. Interfaces* **2017**, *9*, 30267−30272.

16. Van Sickle, A. R.; Miller, J. B.; Moore, C.; Anthony, R. J.; Kortshagen, U. R.; Hobbie, E. K. Temperature Dependent Photoluminescence of Size-Purified Silicon Nanocrystals. *ACS Appl. Mater. & Interfaces* **2013**, *5*, 4233–4238.

17. Miller, J. B.; Usselman, A. C. P.; Anthony, R. J.; Kortshagen, U. R.; Wagner, A. J.; Denton, A. R.; Hobbie, E. K. Phase Separation and the Coffee-Ring Effect in Polymer-Nanocrystal Mixtures. *Soft Matter* **2014**, *10*, 1665–1675.

18. Brown, S. L.; Vogel, D. J.; Miller, J. B.; Inerbaev, T. M.; Anthony, R. J.; Kortshagen, U. R.; Kilin, D. S.; Hobbie, E. K. Enhancing Silicon Nanocrystal Photoluminescence through Temperature and Microstructure. *J. Phys. Chem. C* **2016**, *120*, 18909–18916.

19. Brown, S. L.; Shah, V. D.; Morrell, M. V.; Zubich, M.; Wagner, A.; Denton, A. R.; Hobbie, E. K. Superlattice Formation in Colloidal Nanocrystal Suspensions: Hard-Sphere Freezing and Depletion Effects. *Phys. Rev. E* **2018**, *98*, 062616.

20. Miller, J. B.; Van Sickle, A. R.; Anthony, R. J.; Kroll, D. M.; Kortshagen, U. R.; Hobbie, E. K. Ensemble Brightening and Enhanced Quantum Yield in Size-Purified Silicon Nanocrystals, *ACS Nano* **2012**, *6*, 7389−7396.

21. Miller, J. B.; Dandu, N.; Velizhanin, K. A.; Anthony, R. J.; Kortshagen, U. R.; Kroll, D. M.; Kilina, S.; Hobbie, E. K. Enhanced Luminescent Stability through Particle Interactions in Silicon Nanocrystal Aggregates. *ACS Nano* **2015**, *9*, 9772–9782.

22. Mazzaro, R.; Romano, F.; Ceroni, P. Long-Lived Luminescence of Silicon Nanocrystals: From Principles to Applications. *Phys. Chem. Chem. Phys*. **2017**, *19*, 26507−26526.

23. Yu, Y.; Fan, G.; Fermi, A.; Mazzaro, R.; Morandi, V.; Ceroni, P.; Smilgies, D.-M.; Korgel, B. A. Size-Dependent Photoluminescence Efficiency of Silicon Nanocrystal Quantum Dots. *J. Phys. Chem. C* **2017**, *121*, 23240–23248.

24. Hannah, D. C.; Yang, J.; Podsiadlo, P.; Chan, M. K.; Demortiere, A.; Gosztola, D. J.; Prakapenka, V. B.; Schatz, G. C.; Kortshagen, U.; Schaller, R. D. On the Origin of

Photoluminescence in Silicon Nanocrystals: Pressure-Dependent Structural and Optical Studies. *Nano Lett.* **2012**, *12*, 4200–4205.

25. Mastronardi, M. L.; Maier-Flaig, F.; Faulkner, D.; Henderson, E. J.; Kübel, C.; Lemmer, U.; Ozin, G. A. Size-Dependent Absolute Quantum Yields for Size-Separated Colloidally-Stable Silicon Nanocrystals. *Nano Lett.* **2012**, *12*, 337–342.

26. Greben, M.; Khoroshyy, P.; Liu, X.; Pi, X.; Valenta, J. Fully Radiative Relaxation of Silicon Nanocrystals in Colloidal Ensemble Revealed by Advanced Treatment of Decay Kinetics. *J. Appl. Phys.* **2017**, *122*, 034304.

27. Wen, X.; Zhang, P.; Smith, T. A.; Anthony, R. J.; Kortshagen, U. R.; Yu, P.; Feng, Y.; Shrestha, S.; Coniber, G.; Huang, S. Tunability Limit of Photoluminescence in Colloidal Silicon Nanocrystals. *Sci. Rep*. **2015**, *5*, 12469.

28. Jurbergs, D.; Rogojina, E.; Mangolini, L.; Kortshagen, U. Silicon Nanocrystals with Ensemble Quantum Yields Exceeding 60 %. *Appl. Phys. Lett.* **2006**, *88*, 233116.

29. Sangghaleh, F.; Sychugov, I.; Yang, Z.; Veinot, J. G. C.; Linnros, J. Near-Unity Internal Quantum Efficiency of Luminescent Silicon Nanocrystals with Ligand Passivation. *ACS Nano* **2015**, *9*, 7097–7104.

30. Pringle, T. A.; Hunter, K. I.; Brumberg, A.; Anderson, K.; Fagan, J. A.; Thomas, S. A.; Petersen, R. J.; Sefannaser, M.; Han, Y.; Brown, S. L.; *et al*., Bright Silicon Nanocrystals from a Liquid Precursor: Quasi-Direct Recombination with High Quantum Yield. *ACS Nano* **2020**, *14*, 3858–3867.

31. Yang, Z.; De los Reyes, G. B. Titova, L. V.; Sychugov, I.; Dasog, M.; Linnros, J.; Hegmann, F. A.; Veinot, J. G. C. Evolution of the Ultrafast Photoluminescence of Colloidal Silicon Nanocrystals with Changing Surface Chemistry. *ACS Photonics* **2015**, *2*, 595–605.

32. Brown, S. L.; Miller, J. B.; Anthony, R. J.; Kortshagen, U. R.; Kryjevski, A.; Hobbie, E. K. Abrupt Size Partitioning of Multimodal Photoluminescence Relaxation in Monodisperse Silicon Nanocrystals. *ACS Nano* **2017**, *11*, 1597–1603.

33. Hannah, D. C.; Yang, J.; Kramer, N. J.; Schatz, G. C.; Kortshagen, U. R.; Schaller, R. D. Ultrafast Photoluminescence in Quantum-Confined Silicon Nanocrystals Arises from an Amorphous Surface Layer. *ACS Photonics* **2014**, *1*, 960–967.

34. Kůsová, K.; Ondič, L.; Pelant, I. Comment on "Ultrafast Photoluminescence in Quantum-Confined Silicon Nanocrystals Arises from an Amorphous Surface Layer." *ACS Photonics* **2015**, *2*, 454-455.

35. Ondič, L.; Kusová, K.; Ziegler, M.; Fekete, L.; Gärtnerová, V.; Cháb, V.; Holý, V.; Cibulka, O.; Herynková, K.; Gallart, M.; Gilliot, P.; Hönerlage, B.; Pelant, I. A Complex

Study of the Fast Blue Luminescence of Oxidized Silicon Nanocrystals: The Role of the Core. *Nanoscale* **2014**, *6*, 3837−3845.

36. Dohnalová, K.; Poddubny, A. N.; Prokofiev, A. A.; de Boer, W. D. A. M.; Umesh, C. P.; Paulusse, J. M. J.; Zuilhof, H.; Gregorkiewicz, T. Surface Brightens Up Si Quantum Dots: Direct Bandgap-Like Size-Tunable Emission. *Light: Sci. Appl.* **2013**, *2*, e47.

37. Dohnalova, K.; Gregorkiewicz, T.; Kusova, K. Silicon Quantum Dots: Surface Matters. *J. Phys.-Cond. Matt.* **2014**, *26*, 173201.

38. Kůsová, K. Silicon Nanocrystals: From Indirect to Direct Bandgap. *Phys. Status Solidi A*, **2018**, *215*, 1700718.

39. Kim, K.; Yoo, D.; Choi, H.; Tamang, S.; Ko, J.-H.; Kim, S.; Kim, Y.-H.; Jeong, S. Halide-Amine Co-Passivated Indium Phosphide Colloidal Quantum Dots in Tetrahedral Shape. *Angew. Chem., Int. Ed*. **2016**, *55*, 3714−3718.

40. Guo, J.; Mannodi-Kanakkithodi, A.; Sen, F. G.; Schwenker, E.; Barnard, E. S.; Munshi, A.;Sampath, W.; Chan, M. K. Y.; Klie, R. F. Effect of Selenium and Chlorine Co-Passivation in Polycrystalline CdSeTe Devices. *Appl. Phys. Lett.* **2019**, *115*, 153901.

41. Anthony, R. J.; Rowe, D. J.; Stein, M.; Yang, J.; Kortshagen, U. Routes to Achieving High Quantum Yield Luminescence from Gas-Phase-Produced Silicon Nanocrystals. *Adv. Funct. Mater.* **2011**, *21*, 4042–4046.

42. Mangolini, L. Synthesis, Properties, and Applications of Silicon Nanocrystals. *J. Vac. Sci. Technol. B* **2013**, *31*, 0801.

43. Carlborg, C. F.; Haraldsson, T.; Oberg, K.; Malkoch, M.; van der Wijngaart, W. Beyond PDMS: Off-stoichiometry Thiol-ene (OSTE) Based Soft Lithography for Rapid Prototyping of Microfluidic Devices. *Lab Chip* **2011**, *11*, 3136−3147.

44. Wang, Y. A.; Li, J. J.; Chen, H. Y.; Peng, X. G. Stabilization of Inorganic Nanocrystals by Organic Dendrons. *J. Am. Chem. Soc.* **2002**, *124*, 2293−2298.

45. Barkhouse, D. A. R.; Pattantyus-Abraham, A. G.; Levina, L.; Sargent, E. H. Thiols Passivate Recombination Centers in Colloidal Quantum Dots Leading to Enhanced Photovoltaic Device Efficiency. *ACS Nano* **2008**, *2*, 2356−2362.

46. Turo, M. J.; Macdonald, J. E. Crystal-Bound *vs* Surface-Bound Thiols on Nanocrystals. *ACS Nano* **2014**, *8*, 10205−10213.

47. Kortshagen, U. R.; Sankaran, R. M.; Pereira, R. N.; Girshick, S. L.; Wu, J. J.; Aydil, E. S. Nonthermal Plasma Synthesis of Nanocrystals: Fundamental Principles, Materials, and Applications. *Chem. Rev.* **2016**, *116*, 11061–11127.

48. Liu, X.; Zhang, Y.; Yu, T.; Qiao, X.; Gresback, R.; Pi, X.; Yang, D. Optimum Quantum Yield of the Light Emission from 2 to 10 nm Hydrosilylated Silicon Quantum Dots. *Part. Part. Syst. Charact*. **2016**, *33*, 44–52.

49. Fujii, M.; Minamia, A.; Sugimoto, H. Precise Size Separation of Water-Soluble Red-to-Near-Infrared-Luminescent Silicon Quantum Dots by Gel Electrophoresis. *Nanoscale* **2020**, *12*, 9266-9271.

50. Yu, Y.; Fan, G.; Fermi, A.; Mazzaro, R.; Morandi, V.; Ceroni, P.; Smilgies, D.-M.; Korgel, B. A. Size-Dependent Photoluminescence Efficiency of Silicon Nanocrystal Quantum Dots. *J. Phys. Chem. C* **2017**, *121*, 23240–23248.

51. Miller, J. B.; Harris, J. M.; Hobbie, E. K. Purifying Colloidal Nanoparticles through Ultracentrifugation with Implications for Interfaces and Materials. *Langmuir* **2014**, *30*, 7936–7946.

52. Mastronardi, M. L.; Hennrich, F.; Henderson, E. J.; Maier-Flaig, F.; Blum, C.; Reichenbach, J.; Lemmer, U.; Kübel, C.; Wang, D.; Kappes, M. M.; Ozin, G. A. Preparation of Monodisperse Silicon Nanocrystals Using Density Gradient Ultracentrifugation. *J. Am. Chem. Soc.* **2011**, *133*, 11928–11931.

53. Brown, S. L.; Krishnan, R.; Elbaradei, A.; Sivaguru, J.; Sibi, M. P.; Hobbie, E. K. Origin of Stretched-Exponential Photoluminescence Relaxation in Size-Separated Silicon Nanocrystals. *AIP Advances* **2017**, *7*, 055314.

54. van Dam, B.; Bruhn, B.; Kondapaneni, I.; Dohnal, G.; Wilkie, A.; Křivánek, J.; Valenta, J.; Mudde, Y. D.; Schall, P.; Dohnalová, K. Quantum Yield Bias in Materials with Lower Absorptance. *Phys. Rev. Applied* **2019**, *12*, 024022.

55. van Driel, A. F.; Nikolaev, I. S.; Vergeer, P.; Lodahl, P.; Vanmaekelbergh, D.; Vos, W. L. Statistical Analysis of Time-Resolved Emission from Ensembles of Semiconductor Quantum Dots: Interpretation of Exponential Decay Models. *Phys. Rev. B* **2007**, *75*, 035329.

56. Hartel, A. M.; Gutsch, S.; Hiller, D.; and Zacharias, M. Fundamental Temperature-Dependent Properties of the Si Nanocrystal Band Gap. *Phys. Rev. B* **2012**, 85, 165306.

57. Jakob, M.; Javadi, M.; Veinot, J. G. C.: Meldrum, A.; Kartouzian, A.; Heiz, U. Ensemble Effects in the Temperature-Dependent Photoluminescence of Silicon Nanocrystals. *Chem. Eur. J.* **2019**, *25*, 3061–3067.

58. Brongersma, M. L.; Kik, P. G.; Polman, A.; Min, K. S.; Atwater, H. A. Size-Dependent Electron-Hole Exchange Interaction in Si Nanocrystals. *Appl. Phys. Lett*. **2000**, *76*, 351–353.

59. Hybertsen, M. S. Absorption and Emission of Light in Nanoscale Silicon Structures. *Phys. Rev. Lett.* **1994**, *72*, 1514–1517.

60. Lee, B. J.; Luo, J.-W.; Neale, N. R.; Beard, M. C.; Hiller, D.; Zacharias, M.; Stradins, P.; Zunger, A. Quasi-Direct Optical Transitions in Silicon Nanocrystals with Intensity Exceeding the Bulk. *Nano Lett.* **2016**, *16*, 1583−1589.

61. Davies, G. Radiative Processes in Bulk Crystalline Silicon. *J. Lumin.* **1999**, *80*, 1–7.

62. Cullis, A. G.; Canham, L. T.; Calcott, P. D. J. The Structural and Luminescence Properties of Porous Silicon. *J. Appl. Phys*. **1997**, *82*, 909–965.

63. Iyer, G. R. S.; Hobbie, E. K.; Guruvenket, S.; Hoey, J. M.; Anderson, K. J.; Lovaasen, J.; Gette, C.; Schulz, D. L.; Swenson, O. F.; Elangovan, A. Solution-Based Synthesis of Crystalline Silicon from Liquid Silane through Laser and Chemical Annealing. *ACS Appl. Mater. Interfaces* **2012**, *4*, 2680−2685.

64. Mangolini, L.; Thimsen, L.; Kortshagen, U. High-Yield Plasma Synthesis of Luminescent Silicon Nanocrystals. *Nano Lett.* **2005**, *5*, 655−659.

CHAPTER 6. BIMODAL PL RELAXATION

The PL relaxation is described by the bimodal expression

$$I(t) = I_f \exp\left[-\left(\frac{t}{\tau_f}\right)^{\alpha_f}\right] + I_s \exp\left[-\left(\frac{t}{\tau_s}\right)^{\alpha_s}\right]. \tag{6.1}$$

The integrated intensity (QY) contains two terms: $\Phi = \Phi_s + \Phi_f$, where

$$\Phi_i = I_i \int_0^\infty \exp\left[-\left(\frac{t}{\tau_i}\right)^{\alpha_i}\right] dt. \tag{6.2}$$

The above expression can be rewritten as

$$\Phi_i = I_i \tau_i \frac{\Gamma(\alpha_i^{-1})}{\alpha_i} = \phi_i \left(\frac{\tau_i}{\tau_{i_R}}\right) \frac{\Gamma(\alpha_i^{-1})}{\alpha_i}. \tag{6.3}$$

where ϕ_i, τ_i, and τ_{i_R} are the fraction of emitters, PL lifetime, and radiative lifetime, respectively, of channel *i* (*i* = *s* or *f*, $\phi_s + \phi_f = 1$) and $\Gamma(x)$ is the gamma function. The QY is

$$\Phi = \Phi_s + \Phi_f = I_s \tau_s \frac{\Gamma(\alpha_s^{-1})}{\alpha_s} + I_f \tau_f \frac{\Gamma(\alpha_f^{-1})}{\alpha_f}. \tag{6.4}$$

For $\alpha_i = 1$ (mono-exponential relaxation) this simplifies to the usual expression:

$$\Phi = I_s \tau_s + I_f \tau_f = \phi_s \left(\frac{\tau_s}{\tau_{s_R}}\right) + \phi_f \left(\frac{\tau_f}{\tau_{f_R}}\right). \tag{6.5}$$

For the normalization used here, $A_s = I_s/(I_s + I_f)$ and $A_f = I_f/(I_s + I_f)$, and the ratio Φ_s/Φ_f can thus be expressed in terms of measured quantities as

$$\frac{\Phi_s}{\Phi_f} = \left(\frac{A_s}{A_f}\right)\left(\frac{\tau_s}{\tau_f}\right)\left(\frac{\alpha_f}{\alpha_s}\right)\frac{\Gamma(\alpha_s^{-1})}{\Gamma(\alpha_f^{-1})}. \tag{6.6}$$

The slow mode dominates the QY, as demonstrated in Figure 5.7b, and we thus have $\Phi \approx \left(\frac{\tau_s}{\tau_{s_R}}\right) \frac{\Gamma(\alpha_s^{-1})}{\alpha_s} \propto \tau_s/\tau_{s_R}$.

APPENDIX. SIZE SEPARATION USING THE DGU TECHNIQUE

For DGU, the centrifugation tube is filled gradually with layers of a mixture of chloroform:m-xylene at different percentages (50%, 60%, 70%, 80%, and 90% chloroform), so each layer has a different density than the others. When the tube is filled, the process starts from the bottom of the test tube (highest density, approximately 1.427 g/mL) and goes to the top (lowest density, about 1.177 g/mL). Then the sample is layered on top of the lowest-density layer as shown in **Figure A.1a**. Silicon's density is approximately 2.3290 g/mL. Then another tube is prepared by using the same procedures, except that the last layer is 50% chloroform:m-xylene instead of the sample. The extra tube is called the balance tube. After the spinning is finished, the fractions are collected from the centrifugation tube and stored in 2-mL vials, as shown in **Figure A.1b**.

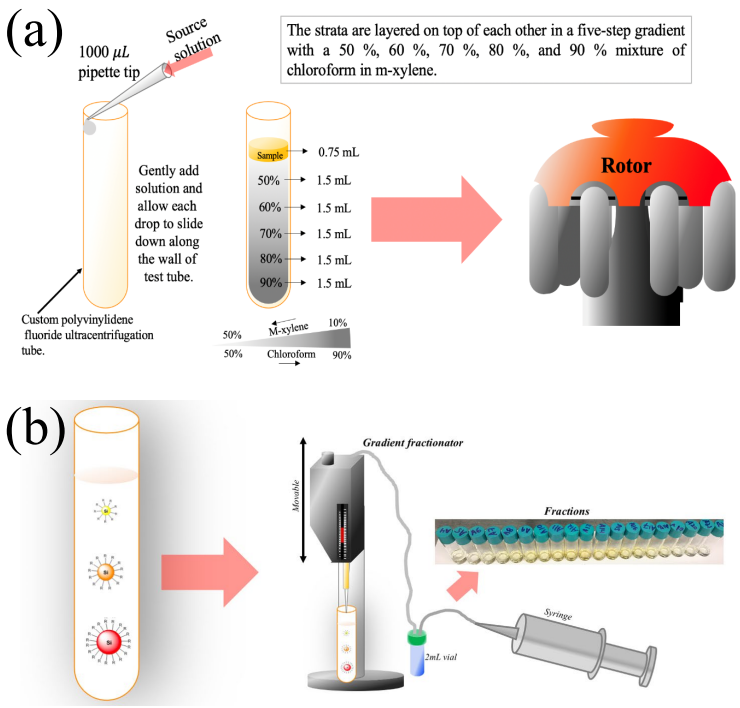

Figure A.1: (a) Steps to prepare the centrifuge tube for DGU. (b) Extracting the fractions from the centrifuge tube.